Thesis for the degree of Doctor of Philosophy

Binding Energies and Lifetimes in Negative Ions

Julia Karls

UNIVERSITY OF GOTHENBURG

Department of Physics
University of Gothenburg
Gothenburg, 2024

© Julia Karls, 2024

ISBN: 978-91-8069-665-4 (PRINT)
ISBN: 978-91-8069-666-1 (PDF)
URL: http://hdl.handle.net/2077/80001

Department of Physics
University of Gothenburg
SE-412 96 Gothenburg, Sweden

Typeset using LaTeX
Figures created using Python, MATLAB and Affinity Designer

Printed by Stema Specialtryck AB
Borås, Sweden, 2024

Trycksak
3041 0234

"If you're referring to the incident with the dragon, I was barely involved."

- Gandalf, *The fellowship of the ring,*
by J.R.R. Tolkien

Abstract

Negative ions hold significant interest because of their importance in understanding electron correlation. Further, they capture substantial focus for their role in, for example: stellar environments, medical applications, antimatter research, and accelerator mass spectrometry (AMS).

This thesis covers experimental studies of both the structure and dynamics of negative ions at the ion beam facilities DESIREE (Double ElectroStatic Ion Ring ExpEriment), CERN-ISOLDE (Isotope Separator OnLine DEvice) and GUNILLA (Gothenburg University Negative Ion and Laser LAboratory).

At DESIREE, the electron affinites (EA) for the three stable isotopes of silicon have been measured with high precision, using laser-manipulation of quantum-state populations followed by laser photodetachment threshold (LPT) spectroscopy. The corresponding isotope shifts in the EA have been calculated. Additionally, the hyperfine splitting of the ground state in $^{29}Si^-$ was measured.

The EA for two radioactive isotopes, ^{128}I and ^{211}At, have been determined using LPT spectroscopy with the GANDALPH (Gothenburg ANion Detector for Affinity measurements by Laser PHotodetachment) detector at ISOLDE. These are the first ever EA measurements of radioactive isotopes. This opens up a whole new field of experiments where the EA of even heavier ions can be measured, and giving the possibility of measuring isotope shifts in radioactive isotopes.

At the ion beam facility GUNILLA at the University of Gothenburg, the EA for rubidium has been measured using a state selective detection of the residual atom in the LPT processes. If this selective measurement technique is combined with the possibility of studying radioactive beams at ISOLDE, it can be applied to studies of rare anions, like francium.

In terms of dynamical properties, the radiative lifetimes of excited states in several atomic and molecular anions have been measured at DESIREE and some previously unobserved energy states have been detected. The methods used for detailed studies of the structure of negative ions used in this work lay the foundation for the ultimate goal to map out the lifetimes of all the excited states in negative ions.

The research presented in here shows that it is only by combining structural and dynamical experimental results that it is possible to obtain a complete picture of negative ions. The results shown so far have been used to benchmark theoretical methods, but there are still quite a few discrepancies. By applying the methods used in this work to the full range of elements in the periodic table, and comparing them with theoretical results, it will be possible to enhance our understanding of electron correlation. Of particular interest will be to study the very heavy systems, where relativistic effects play a decisive role.

.

Keywords: Atomic Physics, Electron Correlation, Electron Affinity, Isotope Shifts, Photodetachment, Negative Ions, Anions, Radioisotopes, Laser Photodetachment Spectroscopy, Resonance Ionization, Neutral Particle Detection, Wigner Threshold Law, DESIREE, ISOLDE, CERN, Radiative Lifetimes.

List of publications

I Precision measurements on Si^-

J. Karls, H. Cederquist, N. D. Gibson, J. Grumer, M. Ji, I. Kardasch, D. Leimbach, P. Martini, J. E. Navarro Navarrete, R. Poulose, S. Rosén, H. T. Schmidt, A. Simonsson, H. Zettergren and D. Hanstorp

In manuscript (2024).

II Laser photodetachment of radioactive $^{128}I^-$

S. Rothe, **J. Sundberg**, J. Welander, K. Chrysalidis, T. Day Goodacre, V. Fedosseev, S. Fiotakis, O. Forstner, R. Heinke, K. Johnston, T. Kron, U. Köster, Y. Liu, B. Marsh, A. Ringvall-Moberg, R. E. Rossel, C. Seiffert, D. Studer, K. Wendt and D. Hanstorp

J. Phys. G Nucl. Part. Phys., 44, 104003 (2017), DOI: 10.1088/1361-6471/aa80aa.

III Upgrades of the GANDALPH photodetachment detector towards the determination of the electron affinity of astatine

D. Leimbach, S. Rothe, L. Bengtsson, A. Ringvall-Moberg, **J. Sundberg**, K. Wendt and D. Hanstorp

Nucl. Instrum. Methods Phys. Res. B: Beam Interact. Mater. At., 463, 277–279 (2020), DOI: 10.1016/j.nimb.2019.05.015.

IV The electron affinity of astatine

D. Leimbach, **J. Karls**, Y. Guo, R. Ahmed, J. Ballof, L. Bengtsson, F. Boix Pamies, A. Borschevsky, K. Chrysalidis, E. Eliav, D. Fedorov, V. Fedosseev, O. Forstner, N. Galland, R. F. Garcia Ruiz, C. Granados, R. Heinke, K. Johnston, A. Koszorus, U. Köster, M. K. Kristiansson, Y. Liu, B. Marsh, P. Molkanov, L. F. Pašteka, J. P. Ramos, E. Renault, M. Reponen, A. Ringvall-Moberg, R. E. Rossel, D. Studer, A. Vernon, J. Warbinek, J. Welander, K. Wendt, S. Wilkins, D. Hanstorp and S. Rothe

Nat. Commun. 11, 3824 (2020), DOI: 10.1038/s41467-020-17599-2.

V The electron affinity of rubidium: A state selective measurement

A. Ringvall-Moberg, M. Nichols, J. E. Navarro Navarrete, U. Berzins, V. D'mello, **J. Karls**, D. Lu, Y. Peña Rodríguez, R. Poulose, A. Morales Rodríguez, K. Ravi, M. Ramachandran, V. Zhaunerchyk, D. Hanstorp, and D. Leimbach

Submitted to *J. Phys. B: At. Mol. Opt. Phys.* (2024).

VI Experimental and theoretical studies of the excited states of Ir^-

M. K. Kristiansson, S. Schiffmann, J. Grumer, **J. Karls**, N. de Ruette, G. Eklund, V. Ideböhn, N. D. Gibson, T. Brage, H. Zettergren, D. Hanstorp and H. T. Schmidt

Phys. Rev. A 103, 062806 (2021), DOI: 10.1103/PhysRevA.103.062806.

VII Lifetimes of excited states in Rh^-

J. Karls, J. Grumer, S. Schiffmann, N. D. Gibson, M. Ji, M. K. Kristiansson, D. Leimbach, J. E. Navarro Navarrete, Y. Peña Rodríguez, R. Ponce, A Ringvall-Moberg, H. T. Schmidt, S. E. Spielman, C. W. Walter, T. Brage and D. Hanstorp

In manuscript (2024).

VIII Measurement of the lifetime of a metastable excited state in Bi^-

M. K. Kristiansson, **J. Karls**, N. D. Gibson, D. Hanstorp, H. T. Schmidt and C. W. Walter

Phys. Rev. A 105, L010801, (2022), DOI: 10.1103/PhysRevA.105.L010801.

IX Lifetimes of excited states in P^-, As^- and Sb^-

J. Karls, M. Björkhage, M. Blom, N. D. Gibson, O. Hemdal Lundgren, M. Ji, M. K. Kristiansson, D. Leimbach, J. E. Navarro Navarrete, P. Reinhed, A. Ringvall-Moberg, S. Rosén, H. T. Schmidt, A. Simonsson and D. Hanstorp

In manuscript (2024).

X Lifetimes of excited states of the lanthanum negative ion

C. W. Walter, F. E. Vassallo, **J. Karls**, J. E. Navarro Navarrete, D. Leimbach, O. H. Lundgren, M. K. Kristiansson, M Björkhage, R. D. Thomas, H. Zettergren, H. T. Schmidt, D. Hanstorp and N. D. Gibson

In manuscript (2024).

XI Spontaneous and photo-induced decay processes of WF_5^- and HfF_5^- molecular anions in a cryogenic storage ring

H. Gnaser, M. Martschini, D. Leimbach, **J. Karls**, D. Hanstorp, S. Indrajith, M. Ji, P. Martini, A. Simonsson, H. Zettergren, H. T. Schmidt and R. Golser

J. Chem. Phys. 157, 044304, (2022), DOI: 10.1063/5.0097896.

Reprints were made with permission from the publishers.

Declaration

Paper II and **III** are published under my maiden name, Julia Sundberg, while **Papers I and III - XI** are published under my married name, Julia Karls. My contribution to the publications are specified below:

I Precision measurements in Si^-
I proposed, planned, and prepared this experiment. I coordinated and participated in data taking and did the analysis of the data. I wrote the first draft and lead the work to finalize the manuscript.

II Laser photodetachment of radioactive $^{128}I^-$
I designed and assembled the GANDALPH detector, its ion optics, and the detector. I took part in the preparatory work in installing the chamber at ISOLDE and testing the beamline, and I took part in data taking and data analysis.

III Upgrades of the GANDALPH photodetachment detector towards the determination of the electron affinity of astatine
I participated in preparatory work for the upgrade of GANDALPH.

IV The electron affinity of astatine
I participated in upgrading GANDALPH for this experiment. I also took part in other preparatory work, such as testing targets used for negative ion production at ISOLDE. In addition to this, I participated in data taking, performed the data analysis together with David Leimbach and wrote the manuscript together with three co-authors.

V The electron affinity of rubidium: A state selective measurement

I participated in data taking and shift work during the experiment.

VI Experimental and theoretical studies of the excited states of Ir^-

I proposed and planned this work and participated in preparatory work and data collection. I also assisted in the final stages of the preparation of the manuscript.

VII Lifetimes of excited states in Rh^-

This experiment was proposed and prepared by me. I participated in the data collection and analyzed the data. I wrote the first draft and lead the work to finalize the manuscript.

VIII Measurement of the lifetime of a metastable excited state in Bi^-

I proposed and planned this experiment and participated in the data collection. I also performed data analysis together with two co-authors.

IX Lifetimes of excited states in P^-, As^- and Sb^-

This experiment was proposed and prepared by me. I lead the data collection and analyzed the data. I wrote the first draft of the manuscript.

X Lifetimes of excited states of the lanthanum negative ion

I participated in the collection and analysis of the data for this experiment.

XI Spontaneous and photo-induced decay processes of WF_5^- and HfF_5^- molecular anions in a cryogenic storage ring

I participated in the collection of data during this experiment.

Additional publications

The following papers were prepared during my time as a PhD student, but are not included in the thesis.

I **β-delayed fission of isomers in ^{188}Bi**

B. Andel, A. N. Andreyev, S. Antalic, M. Al Monthery, A. Barzakh, M. L. Bissell, K. Chrysalidis, T. E. Cocolios, J. G. Cubiss, T. Day Goodacre, N. Dubray, G. J. Farooq-Smith, D. V. Fedorov, V. N. Fedosseev, L. P. Gaffney, R. F. Garcia Ruiz, S. Goriely, C. Granados, R. D. Harding, R. Heinke, S. Hilaire, M. Huyse, J. -F. Lemaître, K. M. Lynch, B. A. Marsh, P. Molkanov, P. Mosat, S. Péru, C. Raison, S. Rothe, C. Seiffert, M. D. Seliverstov, S. Sels, D. Studer, **J. Sundberg**, and P. Van Duppen

Phys. Rev. C 102, 014319 (2020), DOI: 10.1103/PhysRevC.102.014319.

II **Large Shape Staggering in Neutron-Deficient Bi Isotopes**

A. Barzakh, A. N. Andreyev, C. Raison, J. G. Cubiss, P. Van Duppen, S. Péru, S. Hilaire, S. Goriely, B. Andel, S. Antalic, M. Al Monthery, J. C. Berengut, J. Bieroń, M. L. Bissell, A. Borschevsky, K. Chrysalidis, T. E. Cocolios, T. Day Goodacre, J.-P. Dognon, M. Elantkowska, E. Eliav, G. J. Farooq-Smith, D. V. Fedorov, V. N. Fedosseev, L. P. Gaffney, R. F. Garcia Ruiz, M. Godefroid, C. Granados, R. D. Harding, R. Heinke, M. Huyse, **J. Karls**, P. Larmonier, J. G. Li, K. M. Lynch, D. E. Maison, B. A. Marsh,

P. Molkanov, P. Mosat, A. V. Oleynichenko, V. Panteleev, P. Pyykkö, M. L. Reitsma, K. Rezynkina, R. E. Rossel, S. Rothe, J. Ruczkowski, S. Schiffmann, C. Seiffert, M. D. Seliverstov, S. Sels, L. V. Skripnikov, M. Stryjczyk, D. Studer, M. Verlinde, S. Wilman, and A. V. Zaitsevskii

Phys. Rev. Lett 127, 192501 (2021), DOI: 10.1103/PhysRevLett.127.192501.

Contents

Chapter 1

Introduction

In the beginning of the 20$^{\text{th}}$ century, the New Zealand physicist Ernest Rutherford explained results of scattering experiments by a theory of the atomic structure of a positively charged nucleus surrounded by electrons with equal, but negative charge [1]. According to his theory, the atom was kept together by the Coulomb attraction between the nucleus and electrons. The theory also proposed that the majority of the atomic weight was concentrated in the nucleus.

The model of Rutherford did not explain some of the apparent issues with instability of such a system. In a classical system like this, the electron would spiral towards the nucleus, which would cause the atomic structure to collapse. This was addressed by the Danish physicist Niels Bohr, who published the first of a series of three papers in 1913 [2–4], presenting the most widespread description of the atom we have today, the Bohr model. In this model, the issue of electrons spiralling into the core was solved by postulating that the electrons only could exist in certain circular orbits, where they moved without losing energy. Bohr used this model to explain the hydrogen emission spectrum, when he introduced the idea of electrons jumping between orbitals by emitting or absorbing photons. In 1922, Bohr was awarded with the Nobel Prize for his work in this field. Even though we know that the Bohr model is extremely simplified, it is still useful as a simple description of the atom.

Around this time, other famous scientists such as Planck, Einstein and Heisenberg made groundbreaking discoveries in the field of atomic physics.

Planck, with his 1901 paper *"Ueber das Gesetz der Energieverteilung im Normalspectrum"* [5], introduced his hypothesis that energy is emitted and absorbed in discrete quantities, paving the way for the development of quantum theory. Einstein, predominantly renowned for his general theory of relativity, also contributed to the early development of quantum physics when he described light as quanta of energy as an explanation of the observed experimental results of the photoelectric effect in his paper *"Über einen die Erzeugung und Verwandlung des Lichtes betreffenden heuristischen Gesichtspunkt"* published in 1905 [6]. This discovery lead to the concept of wave-particle duality presented by de Broglie in 1924 [7]. In 1927, Heisenberg contributed with his paper *"Über den anschaulichen Inhalt der quantentheoretischen Kinematik und Mechanik"* [8], where the uncertainty principle was first introduced, challenging the classical picture where all physical quantities can be measured exactly.

Although the Bohr model was revolutionary in its time, a more comprehensive description of the atom was given by the Schrödinger and Dirac equations [9, 10]. Here, important features such as wave-particle duality, probabilistic interpretation of electron positions, and relativistic effects are included. Schrödinger introduced the non-relativistic wave-like description of the atom, whereas Dirac introduced a relativistic formalism of the problem. Scrödinger's formulation, encapsulated in the Schrödinger equation, explains the atomic structure and the electron behavior in the atom, establishing a foundation for modern quantum physics. However, exact analytical solutions are limited to the simplest cases, which means that numerical approximations are required for most applications.

Around the same time as Bohr's work, another physicist, Sir J.J. Thomson, observed negative ions in gas-discharges for the first time [11]. However, it was not until 1939, when Rupert Wildt presented the idea that photodetachment of H^- could explain the opacity in the atmosphere of the sun [12], that the research on negative ions would acquire significant attention. The photodetachment process is the removal of the extra electron from the ion by the absorption of a photon. The first photodetachment cross section studies were inspired by this observation, and the first laboratory results of the photodetachment cross sections for H^- and D^- were presented in an article by L. M. Branscomb and S. J. Smith in 1955 [13]. Branscomb and Smith also studied O^- and made the first determination of the experimental electron affinity (EA) of O^- in the same year [14].

A first comprehensive review of negative ions was published by H. S. W. Massey in 1938 and the third edition of this book was published in 1979 [15]. Today, more modern reviews by D. J. Pegg [16] and T. Andersen [17], containing both theoretical and experimental studies of negative ions, are available. Further information about the production of negative ions can be found in "A negative ion cookbook" by R. Middleton [18].

Negative ions of molecular species have been studied extensively [19–21], after being observed in interstellar clouds [22], and the EA of many molecular negative ions and negatively charged clusters have been measured [23]. However, in this thesis, it is mainly atomic negative ions in the gas phase that are covered.

In many cases, atomic systems can be described by the Hartree-Fock model [24], where each electron is treated as if it is moving in the average potential created by all the other electrons. The direct interaction between the electrons in the system, known as the electron correlation, is then treated as a perturbation to this approximation. However, this is not an applicable model for describing negative ions, which can rarely be predicted accurately by the Hartree-Fock model. Instead, negative ions must be described by models where the electron correlation is not only a perturbation, but an integral part of the model. This makes studies of negative ions important, since they can be used to benchmark theories where the electron correlation plays a central role.

There is a large difference between negative ions, as compared to either atoms or positive ions, since the extra electron(s) in negatively charged systems lack the long-range Coulomb interaction found in neutral and positive systems. Instead, the electron correlation is the main force keeping the systems together, giving binding energies of negatively charged ions that are significantly lower than those of neutral or positively charged systems. Furthermore, this means that most negative ions only have a few, if any, bound excited states. This also means that negative ions in general do not have any allowed transitions between bound states, and that some elements are even unable to form negative ions [16].

In most cases, the bound excited states in negative ions have the same parity as the ground state and thus the transitions to the ground state cannot occur via electric dipole (E1) transitions. Consequently, the lifetimes of these states are quite long and cannot be studied in single pass experiments. Instead, the excited state lifetimes can be measured,

for example, at a storage ring facility. The first studies of lifetimes in negative ions involved a metastable autodetaching state in He^- [25]. Since this first measurement, the lifetimes of excited states in several negative ions have been studied [26–28]. With today's storage rings, e.g. the Double ElectroStatic Ion Ring ExpEriment (DEISREE) in Stockholm, where negative ions can be stored for more than an hour [28], very long lifetimes can be investigated.

Not all elements can form stable isotopes. In 1896, Henri Becquerel first discovered radioactivity, after being inspired by W. C. Röntgen's discovery of X-rays [29, 30]. The term radioactivity, however, was coined by the Polish physicist M. Skłodowska Curie and her husband P. Curie in their publication of the discovery of polonium [31]. In 1903 the Curies and Becquerel shared the Nobel Prize for their discoveries in radioactivity. Since then, radioactive isotopes have been extensively studied at radioactive ion beam facilities, such as ISOLDE at CERN in Switzerland, at TRIUMF in Canada and GANIL in France [32–34].

Radioactive isotopes are of special interest due to their applications in medicine. The rare ^{211}At isotope is, for example, used in the radio therapeutic field of targeted alpha therapy (TAT) [35], where a radioactive isotope is coupled to an antibody and carried via diffusion to cancerous metastases. Here, they can decay via the emission of an α-particle which damages the cancerous cell while leaving the surrounding healthy tissue unharmed. The ^{211}At isotope has been used in clinical trials that show very promising results [36]. This very interesting application of astatine, and an overview of past, present and planned clinical trials are summarized in a paper by P. Albertsson *et al.* [37].

Astatine is the least abundant naturally occurring element on Earth. In the outer crust of the Earth's land mass, it is estimated that the total abundance of astatine is as small as 70 mg [38]. Several isotopes of this rare element were first discovered around 1940 [39, 40]. Astatine is difficult to produce and today only a few research centers are able to produce it for medical applications, which makes optimization of the handling of this element extremely important [41].

In order to produce negative ions of an element, several different techniques can be used. Negative ion beams can be produced using a charge exchange cell, where positively charged ions are injected into a gas or metal vapour and the negative ions are created by sequential transfer of two electrons. They can also be produced using a Penning

type plasma ion source or using a cesium sputter source.

The anions can then be studied in several types of experiments. The negative ion properties that can be studied can be divided into structural properties, where the EA and the energies of excited states in the ion are studied, and dynamical properties, where the lifetimes of these excited states are measured. Spectroscopic methods of investigating structural properties include laser photodetachment electron spectroscopy (LPES) [42], where the energy of the detached electron is studied and laser photodetachment threshold spectroscopy (LPT) [43]. Another spectroscopic method is the photodetachment microscope, where the detached electron is guided into an imaging detector through an electric field [44]. The kinetic energy of the electron is measured by recording an interference pattern on the detector. This is a powerful technique for measuring the photodetachment threshold, as results with very high precision can be achieved.

This work mainly covers fundamental physics studies using LPT spectroscopy of atomic and molecular negative ions. However, negative ions are interesting in a variety of experimental contexts. One interesting application of negative ions is laser cooling, which is planned to be used for the sympathetic cooling of antiprotons. This is useful when forming ultracold antihydrogen, as the cold negative ions could efficiently cool antiprotons. Antimatter is a hot topic, and recently the question of the effect of gravity on antimatter was finally answered, when the gravitational force on antihydrogen was determined to be consistent with the gravitational force on matter [45]. This groundbreaking discovery not only enhanced our understanding of fundamental physical principles, but also opened up further exploration of the mysteries of the universe.

Negative ions are of great interest to the field of astrophysics. There is a discrepancy between theory and experimental studies of the proportion of negative ions in space as compared to neutral atoms, which is yet to be fully understood. At cryogenically cooled storage rings, such as DESIREE in Stockholm or the Cryogenic Storage Ring (CSR) in Heidelberg [46, 47], conditions comparable to those found in astrophysical contexts can be achieved for experimental investigations. Studying processes like photodetachment and mutual neutralization (MN) could be of interest in the search for a solution to the excessive amount of negative ions in astrophysical studies.

Another important research field is nuclear fusion, which may hold the

secrets necessary to address the terrestrial challenge of sustainable energy sources. The world's energy needs are increasing and the development of fusion reactors is of considerable interest and relevance as a viable and sustainable energy source. In this field, negative ions play an important role as beams of $^2H^-$ will be neutralised and used in the heating neutral beam injectors of TOKAMAK-type fusion reactors, such as the International Thermonuclear Experimental Reactor (ITER) [48].

Turning the focus to marine environments, the study of green fluorescent proteins (GFP), first discovered in the jellyfish *Aequorea victoria*, is a topic of great interest in scientific research and biotechnology. This class of molecules was first isolated and extracted by Shimomura *et al.* in 1962 [49]. GFP has revolutionized biomedical research, for instance, where it can be used to study cancer development, helping to visualize the spread of the cancerous cells. The fluorescent mechanism in these proteins are found in the chromophore, and the anions of these molecules are subject to intense scientific investigation [50]. Ideally, these proteins would be studied in their natural neutral form; however, neutral molecules are not easily handled and contained. Thus, keeping them in their anionic form is the most optimal choice, as this does not fundamentally change the structure of the molecules.

Other types of experiments with negative ions include detachment by an external electric field and electron-ion collision experiments. For example, electron beams have been used in collisional detachment experiments [51, 52], and doubly excited states can be investigated when an incoming external electron is captured by an atom [53].

In this thesis, the described experiments utilize LPT. These types of experiments can be performed in different geometries, either with a crossed (90°) beam geometry, or a co- or counter-propagating geometry where the laser beam and ion beam overlap along the same propagation axis.

To the author's knowledge, no such LPT experiments have been performed on radioactive negative ions prior to this work. Thus, in order to do these types of measurements on radioactive isotopes, the movable beamline GANDALPH (Gothenburg ANion Detector for Affinity measurements by Laser PHotodetachment) was designed and built for the experimental work covering EA measurements of radioactive isotopes at CERN-ISOLDE (Isotope Separator On-Line DEvice).

Apart from the studies of radioactive isoptopes, a majority of the

measurements described in this thesis were performed at the cryogenic storage ring facility DESIREE. At this facility, ions can be stored for long periods of time, which can be useful for certain types of measurements. For example, a method using laser manipulation of quantum levels in order to do high precision measurements of the EA was recently developed [54]. In this work, this novel method was used to measure the EA of $^{28}Si^-$, $^{29}Si^-$ and $^{30}Si^-$ and the corresponding isotope shifts, and the hyperfine splitting of the ground state in $^{29}Si^-$.

As mentioned above, the dynamical properties of negative ions can be studied by lifetime measurements. In these cases the ions need to be stored over a period of time, which can be done either using ion traps or storage rings. Lifetime measurements have been performed at DESIREE in the work for this thesis; similar experiments have been made for example at CSR, where the lifetimes of metastable states in Si^- have been investigated [55].

The work in this thesis covers LPT experiments with atomic and molecular negative ions in the gas phase. Both photodetachment thresholds and excited state lifetimes have been experimentally investigated. **Papers I**, **II**, **IV** and **V** are focused on the structural properties, presenting the EAs of $^{28-30}Si$, ^{128}I and ^{211}At, and Rb, respectively. **Papers VI - XI** are focused on dynamical properties, where decay processes in several atomic and molecular negative ions and have been studied. **Paper III** covers purely instrumental upgrades to the experimental setup used in **Paper II** and **Paper IV**.

Chapter 2

Theoretical background

2.1 Atomic negative ions

Negative ions are unique in the sense that there is no long range Coulomb potential binding the outermost electron as in positive ions or neutral atoms. Instead, the valence electron in a negative ion is bound by an induced dipole potential, described in theoretical models as electron correlation, and the dominating bonding effect is the electron correlation. An atom will become an induced dipole in an external electric field. When an external electron is approaching an atom, the electrons in the atom are pushed towards the opposite side of the atom and thus the atom becomes polarized. In many cases, this induced dipole moment is strong enough to bind the external electron and create a stable negative ion [16]. In most cases, a theoretical treatment of this binding require a model going beyond the independent particle model, which is the normal starting point for theoretical calculations of atomic structure.

A consequence of this is that negative ions will only have a few, if any, bound excited states and almost all transitions in negative ion systems are optically forbidden. Close to 80% of all naturally occurring elements form stable atomic negative ions [56], but only a fraction of them has more than one bound level within the same term. Apart from this, one of the major differences between negative ions and positive ions or neutral atoms is the magnitude of the binding energy, which is typically ten times smaller in negative ions than in neutral systems [15]. This means,

of course, that anionic systems are much more fragile than neutral atoms and positive ions.

2.2 Photodetachment spectroscopy

The photodetachment process is the negative ion equivalent of photoionisation. This is the process of removing an electron in the negative ion, X^-, by interaction with a photon, γ, with high enough energy, resulting in a neutral atom, X, and a free electron, e^-:

$$X^- + \gamma \longrightarrow X + e^-. \tag{2.1}$$

By energy conservation, this process is only possible if the photon energy is larger than or equal to the binding energy of the negative ion. The probability of detachment can be represented by the cross section as a function of the photon energy.

In the photodetachment process, the electron will be removed far away from the residual atom and the resulting effective potential felt by the electron can be approximated by a centrifugal and a polarization term:

$$V_{\text{Eff}}(r) = \frac{l(l+1)}{2r^2} - \frac{\alpha}{2r^4}. \tag{2.2}$$

Here, l is the angular momentum of the outgoing electron, r is the radial coordinate and α is the dipole polarizability of the residual atom. The effective potential is illustrated in Figure 2.1.

At energies close to the threshold, at large values of r, this expression is largely dominated by the centrifugal term. This was realized by Wigner in 1948 [57], who derived an expression describing the shape of the cross section in this energy region. The photodetachment cross section near the photodetachment threshold can thus be described by the Wigner threshold law [57]:

$$\sigma = \begin{cases} a + b(E - E_{Th})^{l+1/2} & \text{for } E \geq E_{Th} \\ a & \text{for } E < E_{Th} \end{cases}, \tag{2.3}$$

where E is the photon energy, E_{Th} is the photodetachment threshold energy, $l = s, p, d, ...$ is the orbital angular momentum of the outgoing

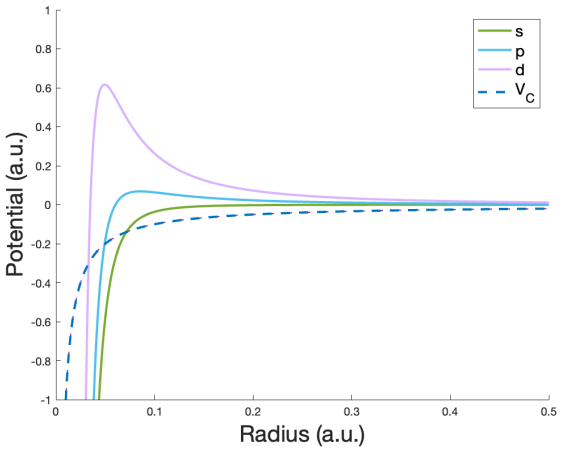

Figure 2.1: The effective potential $V_{\text{Eff}}(r)$ as a function of radius r for different values of the angular momentum, $l = s, p, d$. The Coulomb potential, $V_{\text{C}} \propto -1/r$, is displayed as a dashed line as a reference.

electrons and a and b are constants. The resulting near threshold behaviour will thus be dictated by the leading l-term, as illustrated in Figure 2.2. A threshold with an outgoing s-wave electron is the easiest to determine with a high precision, due to the sharp onset. Ions with p-wave thresholds, on the other hand, can be more difficult to determine with high precision, since the onset is slow. Higher statistics and lower background signal below the threshold are thus crucial to get a high precision measurements.

The detection method used in this thesis is the observation of the residual neutral atom produced in the photodetachment interaction region. Another way of analysing the results would be to observe the outgoing electron and measure for example the energy of the electron or the photoelectron angular distribution [58].

The EA is the binding energy of the negative ion. It is a structural property which can be studied for example using laser photodetachment threshold (LPT) spectroscopy. To date, most elements have (more or less) well-known EAs [56] and an overview of the EAs in the periodic table is shown in Figure 2.3. Some elements cannot form stable negative

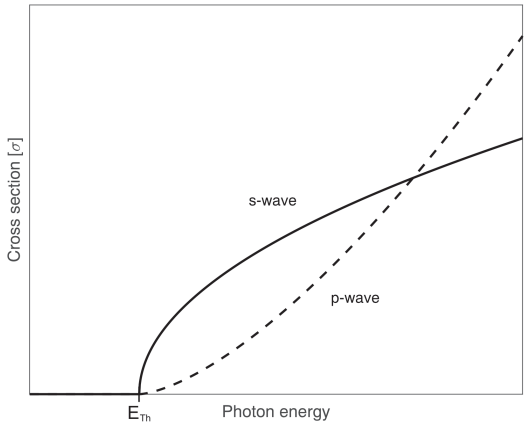

Figure 2.2: The Wigner threshold law for s-wave and p-wave thresholds.

ions and hence can at best only have a metastable negative form, i.e. this means they have negative EAs. In Figure 2.3, these elements are depicted in light grey.

However, there are still some question marks, especially for elements with no stable isotopes, due to the difficulties in producing them and the risks of handling radioactive material. This means they can only be studied in facilities specifically constructed for this purpose.

2.3 Structure

In atomic negative ions, the electronic structure commonly consists of only one or two bound terms, which may be split into two or more fine structure levels. An ion in the ground state can absorb energy, such as from a photon, and move into an excited state. Anions are known in only a few cases to have bound excited states with different parity from the ground state [59–68]. This means that most excited states in negative ions have the same parity in all states and thus exhibit relatively long lifetimes.

The fine structure arises due to the interaction between the magnetic moment of the electrons' spins and their orbital angular momenta, leading to a splitting of the energy term, depending on the total angular

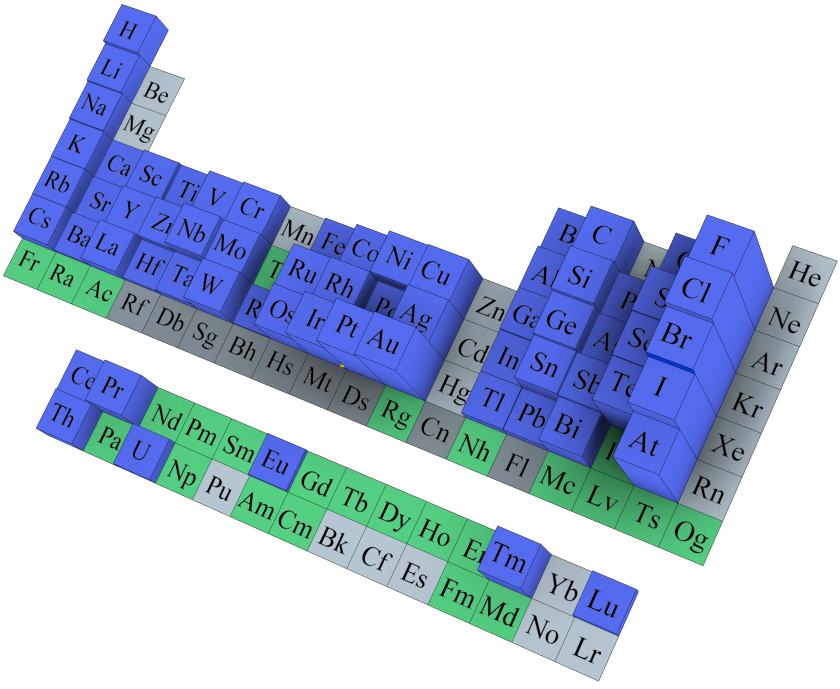

Figure 2.3: Electron affinities (EA) of the elements in the periodic table. The height of each of the blue bars corresponds to the magnitudes of the EAs. Green elements are theoretically predicted to form negative ions but have not yet been experimentally investigated. Elements in light grey are predicted to have negative EAs, whereas dark grey represents elements that neither have been experimentally, nor theoretically, investigated. Figure courtesy of J. Warbinek.

momentum of the electrons in an ion,

$$\mathbf{J} = \mathbf{L} + \mathbf{S}, \tag{2.4}$$

where $\mathbf{L}$ is the orbital angular momentum and $\mathbf{S}$ is the spin angular momentum of the electrons.

The binding energies of excited states are lower than the binding energy of the ground state. In order to use LPTS to study the fine structure of negative ions, the photon energy can be tuned so that photodetachment of only the excited states in the negative ion can occur.

As in the case of the fine structure, the hyperfine structure (HFS) also appears in some isotopes, if the nucleus has non-zero spin. The HFS of the energy levels is due to the interactions between the angular momentum in the electrons ($\mathbf{J}$) and the nuclear spin ($\mathbf{I}$) giving rise to a $\mathbf{F}$-dependent splitting of the levels, where $\mathbf{F}$ is the total angular momentum of the ion,

$$\mathbf{F} = \mathbf{I} + \mathbf{J}. \tag{2.5}$$

This is apparent only in ions with an odd number of nucleons, because in all cases with an even number of nucleons, the nuclear angular momentum $\mathbf{I} = 0$. A schematic overview of an energy level diagram showing fine and HFS is illustrated in Figure 2.4. Each level will show up as a new onset of a Wigner threshold in the photodetachment cross section.

2.3.1 Isotope shifts

In the standard Bohr's and Schrödinger's descriptions of the atom, the nucleus is assumed to be infinitely heavy with no spatial extension. However, the nucleus has a finite mass and volume, and these are different for each isotope of an element. This will affect the structural properties of the ion, and in different isotopes of the same element, the energy levels will be shifted, known as the level shift. Thus, this also gives rise to a shift in the EA for different isotopes.

The mass shift, which occurs due to the change in nuclear mass, is most prominent in lighter isotopes. The other part of the isotope shift is the field shift, which is more pronounced in heavier elements. The field shift arises due to the change in charge distribution in the nucleus.

The electric field caused by the nuclear charge distribution will determine the potential energy of the atomic electrons. This will shift

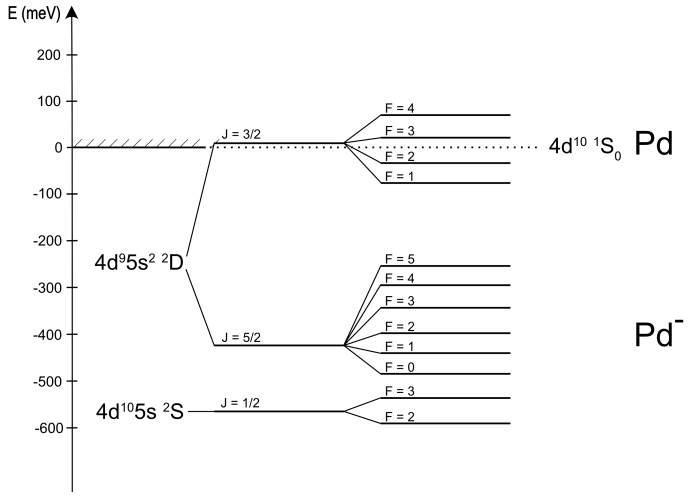

Figure 2.4: Energy level diagram of $^{105}Pd^{-}$ to illustrate the structue in a negative ions with two different electron configurations, term splitting, fine structure and hyperfine structure. $^{105}Pd^{-}$ has $\mathbf{I} = 5/2$, causing the energy levels with $\mathbf{J} \neq 0$ to split into several HFS levels. Note that it is not clear whether the $^2D_{3/2}$ state is bound or unbound [69], and the HFS is not to scale (it is highly exaggerated).

the energy levels for different isotopes and is known as the field shift. The total isotope shift can be expressed as

$$\delta E_{\mathrm{IS}} = \delta E_{\mathrm{MS}} + \delta E_{\mathrm{FS}}, \tag{2.6}$$

where δE_{FS} is the field shift and δE_{MS} is the total mass shift. The mass shift can be divided into two parts, namely the normal mass shift (NMS), and the specific mass shift (SMS):

$$\delta E_{\mathrm{MS}} = \delta E_{\mathrm{NMS}} + \delta E_{\mathrm{SMS}}, \tag{2.7}$$

with δE_{NMS} and δE_{SMS} representing the normal and specific mass shifts, respectively. The NMS is a result of the relative motion of the nucleus and electrons around a common mass centrum and can be easily derived by substituting the electron's mass with its reduced mass. This results

in an NMS of the EA between ions A and B:

$$\delta E_{\mathrm{NMS}} = \frac{m_e(M_A - M_B)}{M_B(M_A - m_e)} E_B, \tag{2.8}$$

where m_e is the electron mass, M_A and M_B ($M_A > M_B$) are the masses of ions A and B, respectively. E_B is the binding energy of a specific energy level in ion B.

The SMS is more complicated to calculate. It arises due to the correlated motion between the electrons in the electron cloud, because of the electrostatic repulsion between them. The SMS is zero if the electrons are totally uncorrelated and move truly independently of each other. If the electrons move in a totally correlated way, the nucleus compensates for this movement and the SMS is large. If the electrons move in an anti-correlated way and are on opposite sides of the nucleaus, the SMS becomes negative. This is typically the case for negative ions, except for the case of H^- [70].

The total isotope shift can be calculated by measuring the EA of the isotopes of interest. The total isotope shift is the difference in EA between these two isotopes. Knowing this value, the SMS for light elements can be calculated by

$$\delta E_{\mathrm{SMS}} = \delta E_{\mathrm{IS}} - \delta E_{\mathrm{NMS}}, \tag{2.9}$$

where δE_{IS} is the measured isotope shift and δE_{NMS} is the normal mass shift derived from Equation 2.8, and trivial to compute. In Equation 2.9 the field shift is assumed to be 0.

The isotope shift has only been measured in a few cases in negative ions and the known isotope shifts are presented in Table 2.1. In the table, the measured total isotope shift is presented, together with the calculated NMS based on the experimental value for the EA and the SMS is the difference between the total isotope shift and the NMS. The field shift is not included, as it is typically very small for lighter elements[1] [71].

[1] In [71] all elements up to neon are considered light. However, in the case of $^{37-35}$Cl the field shift has been calculated to $\sim 0.06\mu$eV [72]. This is still within the error of the total isotope shift and as the field shift for lighter elements than Cl will be smaller, I will in this thesis consider all elements up to Cl as light where the field shift can be neglected.

Table 2.1: Experimentally determined isotope shifts in the EA. The normal mass shift (NMS) is calculated using Equation 2.8 and the specific mass shift (SMS) is the difference between the measured IS and the NMS (assuming the field shift is negligible).

Isotopes	IS (μeV)	NMS (μeV)	SMS (μeV)
$^{2-1}$H	475(44) [70]	205	270(44)
$^{13-12}$C	-9(1)[73]	4.45	-13.5(10)
$^{17-16}$O	-4.1(24) [74]	2.96	-7.1(24)
$^{18-16}$O	-9.266(81) [75]	5.58	-14.85(81)
$^{34-32}$S	0.29(87) [76]	2.09	-1.81(87)
$^{37-35}$Cl	0.91(58) [72]	3.06	-2.15(58)
$^{128-127}$I	Undistinguishable [1]	0.104	N/A

[1] The IS is within the measurement error for ^{128}I and is thus still unknown [77].

2.4 Dynamics

An ion in an excited state will eventually decay to the ground state and emit a photon. The time it takes for half of the ions to decay to a lower-lying state is inversely proportional to the sum of transition rates for the different decay channels.

Since the majority of bound excited states in negative ions have the same parity as the ground state, they cannot decay via allowed, electric dipole (E1) transitions and can only decay via magnetic dipole (M1) or higher order transitions. This means that in negative ions these excited states are usually long lived, and the transitions are almost exclusively parity forbidden. The only exceptions are the cases of Os^- [59–62], Ce^- [63, 64], La^- [62, 65–67] and Th^- [68]. In these ions E1 absorption transitions have been observed.

The selection rules for transitions of the three highest orders, electric dipole (E1), magnetic dipole (M1), electric quadrupole (E2) and magnetic quadrupole (M2), are shown in Table 2.2.

Table 2.2: Selection rules for the four lowest orders of transitions. S is the spin quantum number, L is the orbital angular momentum quantum number, J is the total angular momentum number ($J = L + S$), M_J is the total magnetic quantum number, and π is the parity.

E1	**M1**	**E2**	**M2**
$\Delta S = 0$	$\Delta S = 0$	$\Delta S = 0$	$\Delta S = 0, \pm 1$
$\Delta L = 0, \pm 1$	$\Delta L = 0$	$\Delta L = 0, \pm 1, \pm 2$	$\Delta L = 0, \pm 1, \pm 2$
$(L = 0 \nleftrightarrow 0)$		$(L = 0 \nleftrightarrow 0, 1)$	$(L = 0 \nleftrightarrow 0, 1)$
$\Delta J = 0, \pm 1$	$\Delta J = 0, \pm 1$	$\Delta J = 0, \pm 1, \pm 2$	$\Delta J = 0, \pm 1, \pm 2$
$(J = 0 \nleftrightarrow 0)$	$(J = 0 \nleftrightarrow 0)$	$(J = 0 \nleftrightarrow 0, 1; \frac{1}{2} \nleftrightarrow \frac{1}{2})$	$(J = 0 \nleftrightarrow 0, 1; \frac{1}{2} \nleftrightarrow \frac{1}{2})$
$\Delta M_J = 0, \pm 1$	$\Delta M_J = 0, \pm 1$	$\Delta M_J = 0, \pm 1, \pm 2$	$\Delta M_J = 0, \pm 1, \pm 2$
$\pi_f = -\pi_i$	$\pi_f = \pi_i$	$\pi_f = \pi_i$	$\pi_f = -\pi_i$

2.5 Molecular ions

In this work, mostly atomic negative ions have been investigated, but molecular negative ions is described briefly here. In comparison with atoms, molecules are more complex systems due to, for example, the addition of rotational and vibrational states. This means each energy state also has rotational and vibrational splitting, which opens up a much larger number of excited states within the negative ion, due to the more spacious potential well available to the valence electron.

Just as in the case of atomic anions, molecular anions also have EAs defined as the energy difference between the ground state in the neutral molecule. However, in molecules this transition may not be the most probable one, due to the fact that the removal of the extra electron may cause changes to the geometry or electronic configuration within the molecule, and thus a transition to a rotationally or vibrationally excited state may be more likely. The energy required to remove an electron from an anion, leaving the geometry of the ion unchanged is referred to as the Vertical Detachment Energy (VDE). Similarly, the addition of an extra electron to the ground state in the neutral molecule could change the structure of the negative ion in the ground state. If this is the case,

the more probable transition would be to a ro-vibrational state where the structure is not rearranged, referred to as the Vertical Attachment Energy (VAE).

2.6 Theoretical calculations

Theoretical calculations for negative ions are more complex to perform than for neutral or positively charged systems, since eletron correlation is the cause of their stability. It is therefore of significant interest to directly compare the resemblance of the results from theoretical calculations with results from experimental measurements. In doing so, it is possible to validate or invalidate these theoretical models.

It is a very challenging task to make theoretical calculations for negative ions. Nevertheless, I will present here some very simple calculations, which I then compare with experimental results. For the scope of this thesis, the electron affinity and excited states in Si^- have been investigated with GRASP2018. More comprehensive theoretical calculations are included in many of the papers covered in this thesis, but they have been performed by physicists specialized in theory and therefore provide more extensive theoretical descriptions.

GRASP2018 is based on the fully relativistic multiconfiguration Dirac-Hartree-Fock (MCDHF) method [78]. The calculations presented here are based on a Dirac-Fock (DF) calculation with a gradual increase in the radial orbital to $n = 4$ and $n = 5$. In addition to this, core-valence correlation is added to the $n = 5$ calculation. Here, single excitations from the $2s$ and $2p$ orbitals are included. This core-valence (CV) correlation is added to the already optimized orbitals.

The results of the GRASP2018 calculations for Si^- are presented in Table 2.3. The calculations were performed using core orbitals $1s^2 2s^2$ and with two configurations in the multireference set, $3s^2p^2$ and $3p^4$. The bound energy states in $^{28}Si^-$ are shown in Figure 2.5 and the experimentally measured excitation energies are shown in Table 2.3 as a comparison to the calculated values. Here, we can see that for $n = 5$ the calculated result is within 10% of the experimentally measured value for the $^2D_{3/2}$ and $^2D_{5/2}$ levels and the result differs by just above 10% for the $^2P_{1/2}$ and $^2P_{3/2}$ levels. In Figure 2.6 the resulting energy levels above the $^4S_{3/2}$ ground state are presented for different n levels included in the

Table 2.3: Energy levels for Si^- with electron configuration $3s^2 3p^3$. DF is a pure Dirac-Fock calculation, while column 3 and 4 show values with extended calculations including the radial orbitals $n = 4$ and $n = 5$. These results are compared to experimental energy levels.

State	**DF (eV)**	$n = 4$ **(eV)**	$n = 5$ **(eV)**	**Exp. (eV)**
$^4S_{3/2}$	0.0	0.0	0.0	0.0
$^2D_{3/2}$	1.31542	1.02092	0.93929	0.862287 [79]
$^2D_{5/2}$	1.31670	1.03079	0.94232	0.864032 [79]
$^2P_{1/2}$	1.77238	1.64151	1.50806	1.3605[1] [80]
$^2P_{3/2}$	1.77282	1.63972	1.51337	

[1] Average energy for the $^2P_{1/2}$ and $^2P_{3/2}$ states.

calculations. The dashed lines in Figure 2.6 indicate the experimental values for the $^2D_{3/2}$ (red), $^2D_{5/2}$ (blue) and an average energy for the $^2P_{1/2}$ and $^2P_{3/2}$ levels (black), respectively.

The total energy for the ground state in neutral Si and the total energy for the ground states in Si^- are presented in Table 2.4 and they are plotted as a function of n in Figure 2.7. The EA, which is the difference in total energy for the two systems, is also presented in Table 2.4 for DF and for $n = 4$, $n = 5$ and $n = 5$ + CV. As n increases, the computed value progressively converges towards the experimental value of 1.3895210(7) eV [81]. In order to estimate a span for the actual value of the EA we can compare the $n = 5$ for both neutral and negative Si for the lower limit and compare $n = 5$ for the negative ion with $n = 4$ for the neutral atom for the upper limit. This would place the value of the EA in the interval $1.260 \text{ eV} < \text{EA}(Si^-) < 1.695$ eV, which agrees with the experimental value. This is a large energy range and further improving the calculations would narrow down the interval of the theoretically calculated EA.

The $^2P_{1/2}$ and $^2P_{3/2}$ states are unbound according to these calculations. Since the energy for at least an average of these two states has been experimentally measured [80], it is clear that extending the calculations to $n = 5$ is not enough and the calculations must be extended further.

In an effort to improve the calculations, single excitations from the

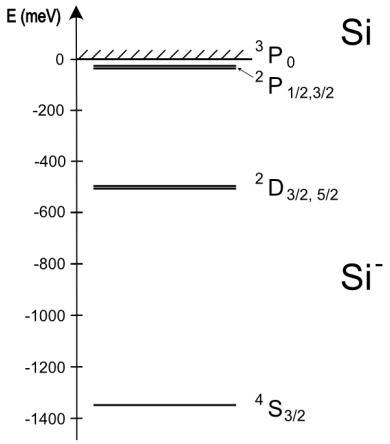

Figure 2.5: The structure of Si^- with experimentally measured energy levels [79–81].

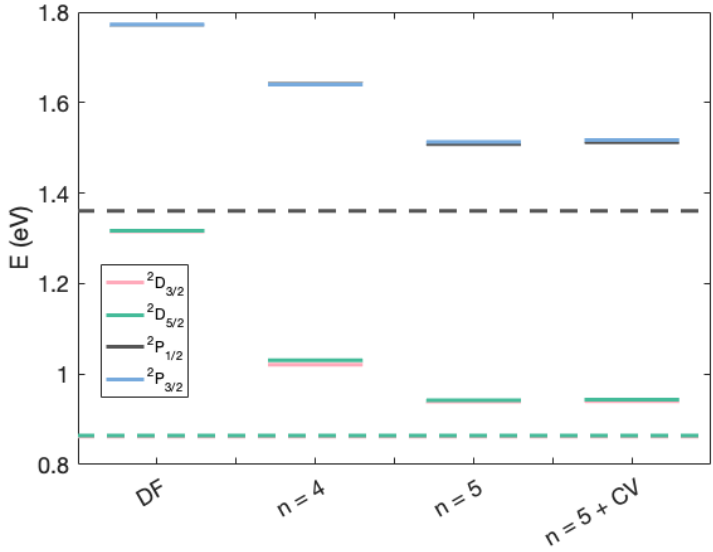

Figure 2.6: Computed energy levels for the excited states in Si^- for increasing radial orbital n. The dashed lines represent the experimental values for the energy levels. DF represents Dirac-Fock calculations and CV represents the addition of core-valence interaction.

Table 2.4: The calculated electron affinity of Si^- for different n. The last column is for $n = 5$ + CV. The experimental value is 1.3895210(7) eV for comparison [81]

Ion	**State**	**DF (a.u.)**	$n = 4$ **(a.u.)**	$n = 5$ **(a.u.)**	**+ CV (a.u.)**
Si	$^3P_0$	-289.4017	-289.4565	-289.4725	-289.4823
Si^-	$^4S_{3/2}$	-289.4255	-289.5003	-289.5188	-289.5271
EA (eV)		0.65	1.19	1.26	1.22

core orbitals are added to both the negative and neutral systems. This is done to introduce core-valence correlations to the calculations. The results for $n = 5$ with the addition of CV correlation are presented in Table 2.5 for the energy levels and the EA can be found in Table 2.4. However, this did not lead to the expected improvement, but rather increased the discrepancy between theory and experiment slightly. This could be due to the core-valence correlation being added to already optimized orbitals, which means the core-valence correlation has not been optimized.

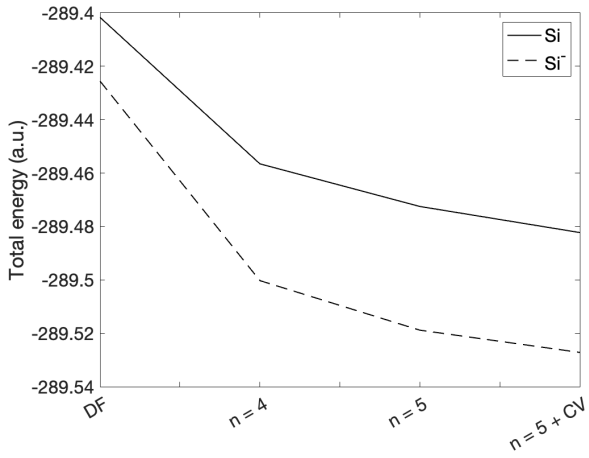

Figure 2.7: Total energy in a.u. for DF, $n = 4$, $n = 5$ and also $n = 5$ with added core-valence correlation.

Table 2.5: Energy levels for Si^- with electron configuration $3s^2 3p^3$ with the addition of core-valence correlation.

State	$n = 5$ **(eV)**	**Exp. (eV)**
$^4S_{3/2}$	0.0	0.0
$^2D_{3/2}$	0.94	0.86 [79]
$^2D_{5/2}$	0.94	0.86 [79]
$^2P_{1/2}$	1.51	1.36[1] [80]
$^2P_{3/2}$	1.52	

[1] Average energy for the $^2P_{1/2}$ and $^2P_{3/2}$ states.

Nevertheless, in Figure 2.7 we can see that with the addition of the core-valence correlation the total energy of both the anionic and neutral systems seem to converge. Small imbalances might lead to amplification of the differences between the two systems and it is very clear that these negative systems are very fragile and sensitive to small variations in the electronic configurations. It is readily apparent that comparing two different systems poses considerable challenges. Experimental results are evidently essential to benchmark theoretical models of negatively charged ions.

Chapter 3

Experimental methods

3.1 Experimental conditions

All experiments presented in this thesis are based on the principle of laser photodetachment of negative ions and the detection of the neutral atoms created by this process. This general method is applied to both EA measurements of radioactive and stable isotopes and lifetime measurements of excited states in negative ions.

In order to perform LPT (laser photodetachment threshold) measurements, a negative ion source, a laser beam and a neutral atom detector are needed. The anions in these experiments are produced either using a cesium sputter source, or a surface ion source. These sources generally produce multiple ion species, and to be certain that the experiments target only the isotope of interest, the specific mass must be selected. This can be done using a mass-selecting magnet and ion optics. The mass-selected ions are guided to the interaction region where the ion beam is overlapped with the laser beam and an electron can be detached. The resulting neutral atom is then detected. To have a reasonable signal-to-noise ratio, the vacuum in the chamber must be very good, where a pressure of 10^{-8} mbar or less is preferred. For lifetime measurements the pressure must be even lower to avoid the ion beam being lost too quickly due to collisions with the residual atmospheric gases.

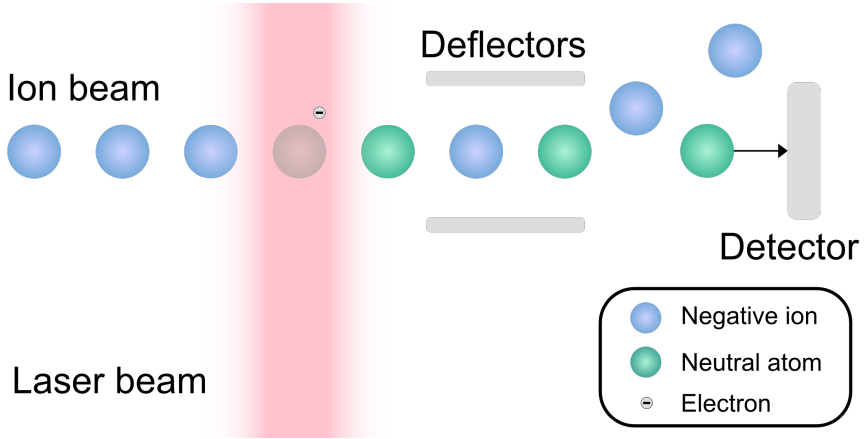

Figure 3.1: This is a figure of a crossed beam geometry photodetachment experiment. Photodetachment is performed in a collinear or crossed beam geometry. Neutral atoms continue along the axis into the detector and negative ions can be deflected by electrostatic potentials.

3.1.1 EA measurements

The electron affinity of a negative ion can be measured using several different approaches. In this thesis the LPT spectroscopy method is used. This can be done in either a collinear setup, with a 0° or 180° angle between the laser and ion beam, or in a crossed beam geometry, with a 90° angle between laser and ion beam. The crossed beam setup is illustrated in Figure 3.1.

The well-defined interaction volume makes the crossed beam geometry ideal for performing absolute cross section measurements. The collinear geometry is preferred for relative cross section measurements, due to the fact that this increases the length of the interaction region and reduces the Doppler broadening [16].

The collinear geometry requires the measurements to be performed in both a co- and counter-propagating setup in order to correct for the Doppler shift. The Doppler shift is corrected by taking the geometric mean of co- and counter-propagated measurements:

$$\sqrt{E_{EA}^{\uparrow\uparrow}E_{EA}^{\uparrow\downarrow}} = \sqrt{\frac{1+v/c}{\sqrt{1-v^2/c^2}}E_{EA}\frac{1-v/c}{\sqrt{1-v^2/c^2}}E_{EA}} = \sqrt{E_{EA}^2} = E_{EA}, \tag{3.1}$$

where $E_{EA}^{\uparrow\uparrow}$ and $E_{EA}^{\uparrow\downarrow}$ are the co- and counter- propagating values for the EA, v is the ion velocity and c is the speed of light.

These experiments use wavelength tunable lasers, where the laser wavelength (and hence photon energy) is tuned in the range of the predicted EA. The photodetachment thresholds are then revolved by measuring the yield of neutral atoms as a function of the laser wavelength. The Wigner threshold law in Equation 2.3 is used to fit the experimental data and the resulting EA can be extracted from this fit.

The isotope shift in the EA can be extracted from the difference in EA for two isotopes. Since the isotope shift is a relative value, the shift can be derived from either the EAs calculated from the geometric mean of co- and counter-propagating measurements, or from measurements performed in one direction only, corrected for the Doppler shift with the relativistic Doppler shift formula, resulting in the center-of-mass frequency, f_{COM}, as perceived by the ions:

$$f_{\mathrm{COM}} = \sqrt{\frac{c-v}{c+v}}f_{\mathrm{Lab}}, \tag{3.2}$$

where c is the speed of light, v is the ion velocity and f_{Lab} is the laser frequency in the laboratory frame. This is valid for a co-propagating setup, while a counter-propagating setup would give opposite signs in Equation 3.2.

3.1.2 Lifetime measurements

In the case of a negative ion with bound excited states, the dynamical properties of the systems can be measured. The radiative lifetimes of excited states can be measured by storing these ions in a beam and measuring the yield of neutrals over time. Since the transitions between the excited states of negative ions are almost exclusively E1 forbidden, the lifetimes can be very long, which means the ions have to be stored for some time in order for the lifetimes to be measured.

In order to measure lifetimes, the ion beam is overlapped with a laser beam, inducing photodetatchment if the photon energy is larger than the energy of the state. The resulting neutral atoms are sent into a detector and the lifetime can be extracted from an exponential decay fit of the number of detected neutrals as a function of time.

In addition to lifetime measurements of bound excited states in the ion, lifetimes of doubly-excited metastable states can also be measured. These states will decay to neutral atoms via autodetachment and require no laser detachment.

3.1.3 Detectors

Common types of detectors used in ion experiments include channel electron multipliers (CEM), microchannel plates (MCPs) and neutral particle detectors. A CEM is an electron multiplier, where an initial electron electron (or ion) is attracted to the entrance of the CEM by a attractive potential and is accelerated towards the back of the CEM by a high positive potential. The CEM is shaped in a way that the particle strikes the interior surface of the CEM, where the electron is multiplied via secondary emission of electrons throughout the tube, which increases the detectable current. An MCP is a plate with several thousand electron multiplier channels which each work in a similar way as a CEM, with the addition of the possibility to add spatial resolution.

For the electron affinity measurements in this thesis, a neutral particle detector is used to detect the residual atoms from photodetatchment [82]. This detector is composed of a conductive glass plate in combination with a CEM that detects the secondary electrons produced when neutral atoms impinge on the plate. The conductive coating on the glass plate surface is essential to avoid charging effects.

3.2 Experimental facilities

The EA measurements of radioactive isotopes were performed using a movable setup at the ISOLDE facility at CERN. The high precision EA and lifetime measurements were performed at the DESIREE storage ring in Stockholm, where it is possible to store ions for more than an hour. Finally, photodetachment studies have been performed at the GUNILLA

facility in Gothenburg.

3.2.1 ISOLDE

ISOLDE stands for Isotope Separator On Line DEvice and it is a radioactive ion beam (RIB) facility, where the isotope separation on-line (ISOL) technique is used to produce RIBs [83]. Different elements can be produced through spallation, fragmentation, or fission when a thick target is bombarded by a 1.4 GeV pulsed proton beam, as depicted in Figure 3.2. The products can then be ionised using a either a surface, plasma, or laser ion source.

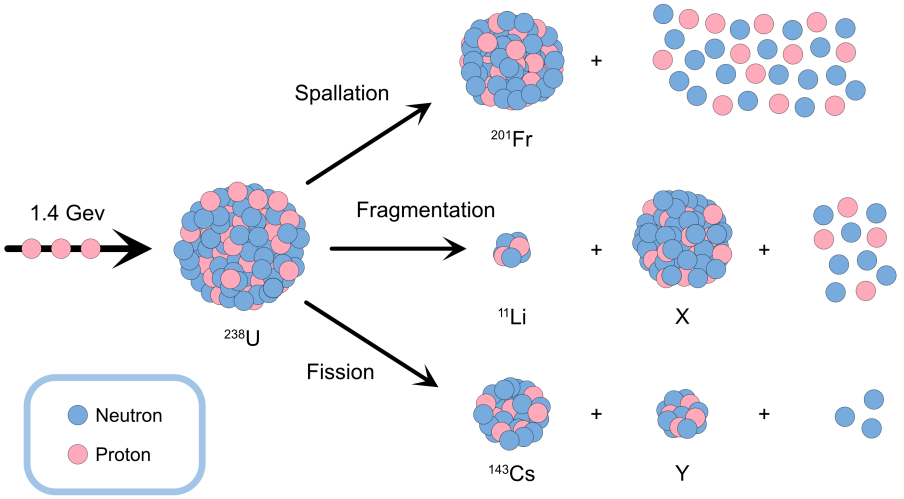

Figure 3.2: A range of elements and radioisotopes can be produced at ISOLDE through one of the processes of spallation, fragmentation, or fission.

The ISOLDE facility has two mass separators: the high resolution separator (HRS) and the general purpose separator (GPS). The GPS has one mass separating magnet, whereas the HRS has two mass separating magnets and thus the mass resolution of the HRS is higher than that of the GPS. From the two separators, the ion beams are guided to the experimental area in the hall where both permanent and movable experimental stations are established.

ISOLDE is normally producing positive ions, but for the EA measurements in this thesis, this was changed to instead produce negative ions. The negative ion production and ion source development at ISOLDE are described in detail in a paper by Liu *et al.* [84]. The setup of the ISOLDE hall is shown in Figure 3.3.

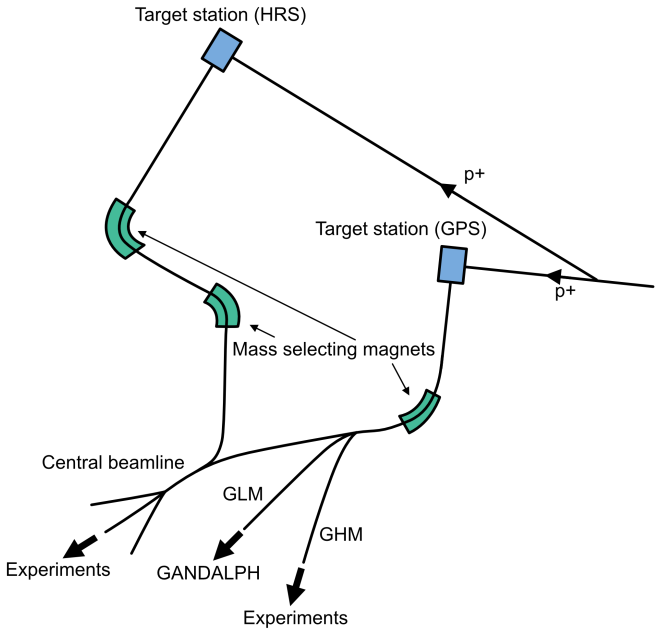

Figure 3.3: Schematic overview of the ISOLDE hall. GHM is the General High Mass beamline, and GLM, the General Low Mass beamline, which is used for the experiments in this works. Here the ions are mass selected before they travel into the GANDALPH detector (Gothenburg ANion Detector for Affinity measurements by Laser Photodetachment).

Negative ion production at ISOLDE

At CERN, protons are accelerated using a linear accelerator (LINAC2) and then injected into the Proton Synchrotron Booster (PSB), where they are further accelerated to an energy of 1.4 GeV and currents of up to 2 μA. These high energy protons are used to bombard a thick Th/Ta mixed foil target at the GPS beamline, which will induce spallation, fission, or fragmentation reactions in the target material. The products in this process are then released into an ion source, and in the case of negative ions, a surface ionizer with a low work function is used. This ionizer is comprised of a hot, tubular transfer line and a LaB_6 surface ionizer pellet heated to 1300°C. LaB_6 is chosen as an ionizer due to its low work function of 2.7 eV. The ions are then accelerated across a 20 kV extraction potential and mass selected in the general purpose mass separator magnet (GPS).

Thereafter, the ions are guided to the experimental area using ion optics. At the experimental area, the ion beam path continues to the General Low Mass (GLM) beamline. This is where the GANDALPH chamber is attached to the ISOLDE beamline and where the interaction region of the experiment is located.

GANDALPH

The original version of the GANDALPH chamber was designed and manufactured at the University of Gothenburg and thereafter transported to CERN, where it was assembled. This was the version of the chamber used for the ^{128}I experiment (Paper II [77]), whereas the ^{211}At experiment (Paper IV [85]) required some upgrades to the chamber and detector (Paper III [86]), which were completed at CERN. A schematic overview of the upgraded version of the GANDALPH detector is shown in Figure 3.4.

The ion beam is injected into the chamber with a 10° bend and overlapped with a co- or counter-propagating laser beam of appropriate photon energy. The interaction region, where the laser beam can strip the ions of their extra electron, is defined by two 6 mm apertures placed 50 cm apart. After the interaction region, the negative ions that are still present in the beam are deflected into a Faraday cup, whereas the photodetached neutral atoms continue straight into the neutral atom detector. This detector is composed of a metal box, with a glass plate

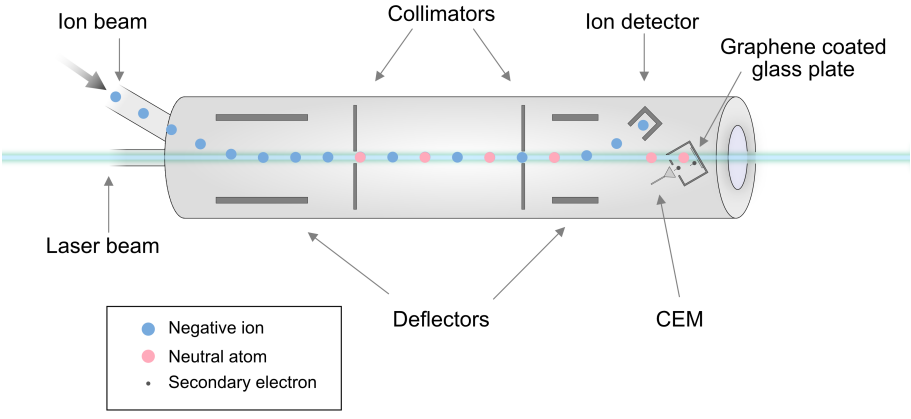

Figure 3.4: Schematic overview of the GANDALPH beamline.

bottom. The glass material is chosen to be transparent to the laser beam and is coated with a conductive material in order to avoid charge up effects. The glass plate was coated with indium tin oxide (ITO) for the ^{128}I experiment, but this was upgraded to graphene on quartz for the ^{211}At experiment in order to decrease the photoelectric effect and increase the transparency for the photons [82]. Upon impingement by a neutral, secondary electrons can be produced and these are guided into a CEM using electrostatic potentials.

Lasers used at ISOLDE

Several types of laser system can be used for LPT experiments, but in general tunable, narrowband lasers are needed since this makes it possible to scan over a wavelength region, e.g. over a photodetachment threshold. Examples of tunable lasers are solid state titanium:sapphire (Ti:Sa) lasers, optical parametric oscillator (OPO) lasers and dye lasers [87–89].

At ISOLDE, lasers from RILIS (Resonance Ionisation Laser Ion Source) were used for both experiments. These lasers are normally used for the production of radioactive positive ions at ISOLDE, but

in our case they were used for laser photodetachment studies. For the EA measurement of ^{128}I, a 10 kHz repetition rate pulsed, tunable titanium-sapphire laser (Ti:Sa) was used [90]. The bandwidth of the laser was 10 GHz. For the ^{211}At experiment the laser beam was generated by a commercial dye laser (Credo Dye, Sirah Laser-und Plasmatechnik GmbH). The dye laser was operated with an ethanol solution of Coumarin 503 dye and it was pumped by the third harmonic output of a pulsed Nd:YAG INNOSLAB laser (CX16III-OE, EdgeWave GmbH), with a pulse repetition rate of 10 kHz, a bandwidth of 12 GHz and a typical pulse duration of 7 ns.

3.2.2 DESIREE

The Double ElectroStatic Ion Ring ExpEriment (DESIREE) is a cryogenic ion beam storage ring where one positive and one negative ion beam can be stored simultaneously and overlapped in an intersecting interaction region. The circumference of each storage ring is 8.7 m and the beamline is kept at a pressure of 10^{-14} mbar at a temperature of 13 K [91]. An overview of the DESIREE facility is shown in Figure 3.5.

In an ion trap, the ions can be confined using electrostatic potentials. This makes the setup compact and versatile, and the motion of the ions can be controlled. This setup also allows for the possibility to isolate and manipulate ions. On the other hand, using a storage ring to study ions has many other advantages to storing ions in a trap. For example, the accessibility for ion interactions with other particles or photons is improved, the Doppler shift is well defined and the collision energies can be controlled. Additionally, the experiments can be performed at keV energies, which allows for higher detection efficiency of the neutral atoms. The main disadvantage of is that a storage ring is a very large and expensive device. The above mentioned advantages, in combination with the ultra-high vacuum and low temperature at DESIREE, make for ideal conditions for performing lifetime measurements of excited states. These studies require very low background collisions since some states are not very well populated.

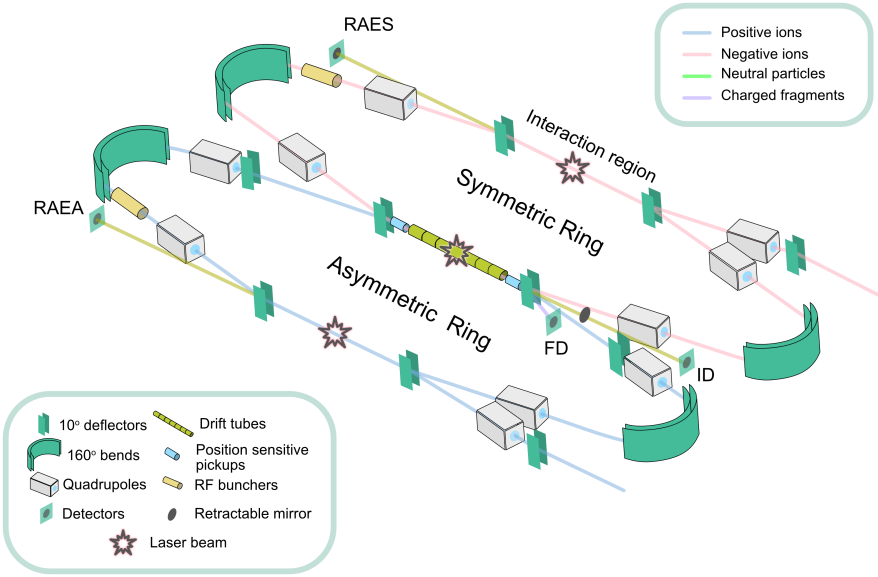

Figure 3.5: Schematic overview of the DESIREE storage rings.

Ion production at DESIREE

The ion source at DESIREE is a SNICS II type source, i.e. a cesium sputter source [92]. This type of ion source is commercially available from National Electrostatics Corporation [93]. The ions produced by a SNICS ion source are very hot, and thus many excited states in the ions will be populated, which is a prerequisite for lifetime measurements. A drawing of the sputter ion source is shown in Figure 3.6.

A powder of a substance containing the element of interest is inserted inside a cavity of a copper or aluminium cathode and placed in the ion source. A cesium reservoir inside the source is heated and the produced cesium vapour is ionised when it condenses on the ionizer surface. These Cs^+ ions can then be accelerated toward the cathode, which is at a negative potential, and sputter the target material. The cathode is cooled, causing some of the Cs atoms to condense on the cathode surface. Due to the low work function of Cs, the sputtered material can then pick up an extra electron from the Cs layer on the cathode surface [94].

Thus, the sputtered atoms become negatively charged and can then be accelerated towards the beamline by a potential difference of 10-30 kV, created by a positively charged extractor electrode. The selected ions are then mass selected by a 90° bending magnet and the ions of interest are focused and guided through a series of ion optics and injected into one of the DESIREE storage rings.

Ion beam storage rings

The ions are transported to the storage rings via the ion beamlines, which hold a vacuum of 10^{-7} mbar close to the ion source and 10^{-10} mbar

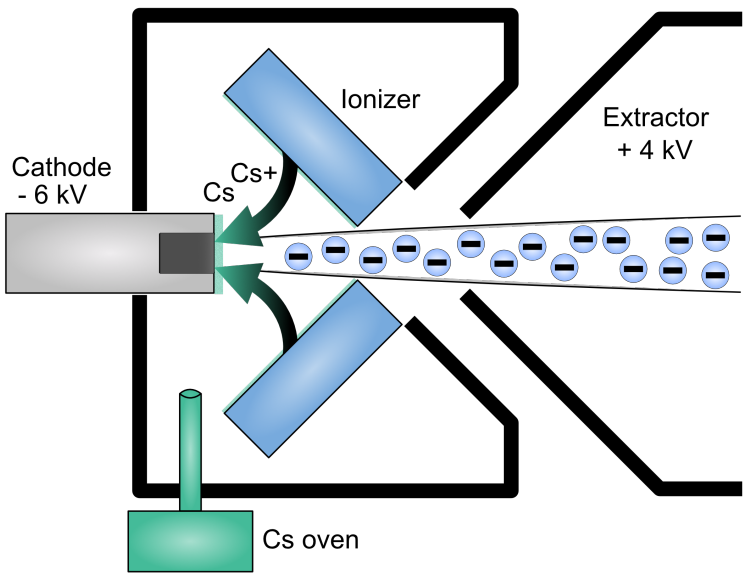

Figure 3.6: A Cs sputter ion source. The Cs oven is a heated Cs reservoir, causing the Cs to vaporize. The Cs atoms are ionised on the ionizer and accelerated towards the cathode sputtering the cathode material. Cs will condense on the cool cathode surface and due to the low work function, the Cs atoms will donate electrons to the sputtered fragments. The negatively charged ions are extracted from the source by an electrostatic potential difference between the source and the extractor.

close to the storage rings. Upon entering one of the storage rings, the ions have a well defined mass and kinetic energy and they enter the ring in bunches separated in time. In our experiments only the symmetric ring is used for ion beam storage. In the symmetric ring, the focusing quadrupoles are placed symmetrically as illustrated in Figure 3.5. In addition to this, the storage ring contains several steering, focusing, and correction elements to keep the ion beam in the storage ring for as long as possible.

The extremely low temperature of $\sim$ 13 K in the storage rings is achieved by using four cryocoolers and the extremely good vacuum of $\sim 10^{-14}$ mbar is achieved by the combination of pumping and cryogenic cooling. Additionally, a new 1 m^2 screen has been installed, cooled to 2.6 K by a cryostat. This new screen is cold enough to freeze hydrogen to the surface [95], reducing the pressure even further. There are no vacuum gauges capable of directly measuring the low pressure inside the chamber, which means the pressure has to be estimated by the ion beam storage time in the ring. There are four mechanisms that cause losses in the ring. First, the injected ions might have a beam divergence larger than the acceptance angle of the ring. These ions are lost during the initial phase of a beam cycle. Second, ions can be lost because of collisions with the rest gas in the chamber, but at DESIREE this loss is minimal due to the very low pressure. However, the lifetime of ions stored in the beam can be used as a probe of the pressure, provided that the beam current is sufficiently low. Third, ions can be lost as a result of ion-ion collisions. Hence, it is essential to keep the ion current as low as possible to reduce this effect. Finally, the ions will be lost due to the photodetachment process, i.e. the process we investigate.

The ion beam current can be monitored with a Faraday cup immediately before injection into the ring or with a Faraday cup when the ions are dumped at the end of storage.

During lifetime measurements, it is essential to keep the ion current as low as possible to reduce losses in the ion beam due to ion-ion interactions. The ion beam current can be monitored with a Faraday cup immediately before injection into the ring or with a Faraday cup when the ions are dumped at the end of storage.

Lasers used at DESIREE

For the experiments at DESIREE, a 10 Hz tunable OPO, a 1 kHz tunable OPO, a CW tunable Matisse Ti:Sa laser and a narrow bandwidth CW SolsTis Ti:Sa laser are used in order to produce the wavelengths needed for photodetahcment of different energy levels.

The Matisse Ti:Sa is tunable between 670-1020 nm and has a bandwidth < 2 MHz and a maximum output power of 1.5 W. It is pumped by a 532 nm Millennia Pro 15s diode laser, which is a frequency doubled neodymium-doped yttrium aluminum garnet (Nd:YAG) laser.

The SolsTis is a CW Ti:Sa laser pumped by an Equinox diode laser at 532 nm with a power up to 18 W. These two systems are from the same manufacturer, M Squared [96]. For the high precision measurements of the EA of the different isotopes of Si^-, this narrow bandwidth Ti:Sa from M Squared is required to achieve a high enough energy resolution to distinguish the isotope shift and the hyperfine structure in $^{29}Si^-$. This laser has a maximum output power of 2.5 W and a bandwidth smaller than 100 kHz. The tuning range is the same as for the Matisse Ti:Sa.

The wavelength of the laser is measured with a HighFinesse WS8-2 wavelength meter, which is re-calibrated several times during the measurements. For the calibration, the dipole forbidden transition $^2S_{1/2} \rightarrow^2 D_{5/2}$ in $^{88}Sr^+$ is used.

In the case of the lifetime measurements, the Ti:Sa lasers are used for total ion beam storage time measurements as the accessible wavelengths for this type of laser are sufficiently short to detach all states of the ions.

The OPOs, on the other hand, are tunable over a larger wavelength region and are used to detach only ions in excited states in all of the lifetime measurements. The 10 Hz OPO is pumped by a Q-switched Nd:YAG pump laser. It has a tuning range of 193-2600 nm and has a pulse length of about 5 ns with a maximum pulse energy of 50 mJ. This laser was mainly used for the measurements that were performed before the 1 kHz OPO was installed. It has a pulse duration of 5 ns with a maximum pulse energy of 600 μJ. This laser is tunable between 210-2600 nm. The bandwidth of both OPO lasers are comparable at 150 GHz.

3.2.3 GUNILLA

The GUNILLA (Gothenburg University Negative Ion and Laser LAboratory) beamline is used for direct current LPT measurements where it is possible to create and detect Rydberg atoms. A conventional PS-120 cesium sputter source from Peabody Scientific is used for ion production. This produces ions using the same principle as the ion source used at DESIREE as described in section 3.2.2. The original design of GUNILLA is described in reference [43], but it has since received multiple upgrades, e.g. the RADAR (Rydberg Atom Detector for Anion Research) and Doppler spectrometers. The current setup is shown in Figure 3.7.

The ions are extracted from the source, accelerated to 6 keV and sent into a mass separating magnet where the ions are mass selected and bent by 90°. The ions are then guided towards one of the interaction regions by ion optics. The ions are guided either into the Doppler or RADAR spectrometers [98]. Here the ions are overlapped in a co- or counter-propagating geometry with one or several laser beams. The available tunable lasers are several OPOs, a Dye laser, and a Ti:Sa laser.

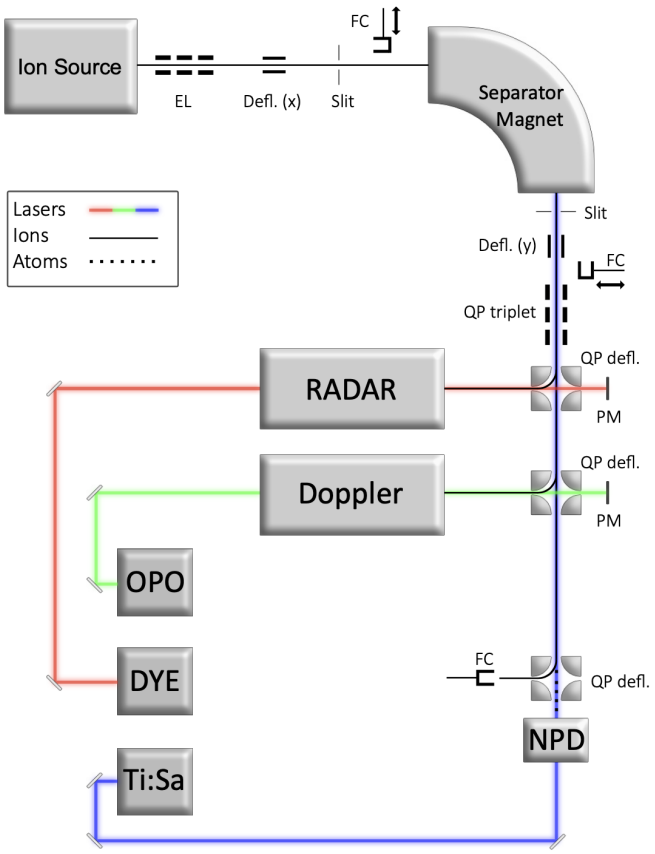

Figure 3.7: The GUNILLA beamline. The Einzel lens (EL), x (horizontal) and y (vertical) direction deflectors (Defl.), quadrupole triplet (QP triplet), and quadrupole deflectors (QP defl.) guide the ion beam to three distinct spectrometers: RADAR, Doppler, or NPD. Retractable Faraday cups (FC) are used to measure the beam current. High-intensity lasers, including OPO, Dye, and Ti:Sa lasers, deliver laser beams to the various experimental setups via optical mirrors. During experiments, the laser power is monitored using movable power meters (PM). Figure courtesy of A. Ringvall-Moberg [97].

Chapter 4

Results and discussion

4.1 Part I - EA measurements

The first part of this chapter covers structural investigations of negative ions in the form of EA measurements. These measurements were all performed using LPT spectroscopy and were performed at three different facilities: DESIREE in Stockholm, CERN-ISOLDE in Geneva and GUNILLA in Gothenburg. At DESIREE, high precision measurements were performed, using manipulation of the quantum levels of stored negative ions. At ISOLDE, the EAs of radioactive isotopes were investigated and at GUNILLA, LPTS combined with RIS to selectively photodetach ions in a specific state. The following presents the key results from Paper I-V.

4.1.1 High precision measurements of Si^- at DESIREE

High precision EA measurements of Si isotopes at DESIREE

In this experiment, 25 keV Si^- ions were stored in the symmetric storage ring at DESIREE. On one side of the storage ring the ion beam was overlapped with a narrow bandwidth continuous wave (cw) Ti:Sa laser. The lasers are described in Section 3.2.2. The laser was overlapped with the ion beam in both a co- and counter-propagating geometry; the

direction of the laser beam path was controlled using a flip mirror.

On the other side of the storage ring, known as the merging section, the ion beam was overlapped with a high power diode laser at 1053 nm (a wavelength set to detach the extra electron from the excited states of Si^-, but not the ground state), and thus depleting the ions in excited states. The laser beam was reflected on a mirror at the end of the merging section and thus it overlaps twice with the ion beam and the laser beam path comes to an end outside of the chamber.

This laser depletes the stored ion beam of ions in excited states for 30 seconds in the beginning of the cycle, leaving an ion beam consisting of almost solely ions in the ground state. This reduces the background from excited states significantly, allowing a much higher precision of the EA onset to be achieved. This method was recently developed at DESIREE, and has resulted in the highest precision EA measurement to date [54].

Subsequent to each ion beam injection into the storage ring, the measurement cycle was as follows: The ion beam enters the storage ring and the ions in excited states are exposed to the depletion laser for 30 seconds. After this, the wavelength of the narrow bandwidth laser was scanned over the estimated ground state threshold up to six times per cycle after which the ion beam was dumped and a new injection takes place. The timing scheme of one measurement cycle is illustrated in Figure 4.1, and the Si^- structure and laser scheme are illustrated in Figure 4.2.

The EAs and corresponding isotope shifts were measured for the three stable isotopes of Si: ^{28}Si (92.5%), ^{29}Si (4.7%) and ^{30}Si (3.1%), with natural abundances given in the parentheses. In order to get absolute values of the EAs of all three isotopes, multiple experiments have to be carried out, varying the direction of the laser beam between co- and counter-propagating using a flip mirror between each measurement. For these measurements, three injections were done in each cycle before the direction of the laser beam was changed. In addition to this, the hyperfine structure of the $^{29}Si^-$ isotope specifically has been investigated. The results for these measurements are presented in Table 4.1 and in the following sections.

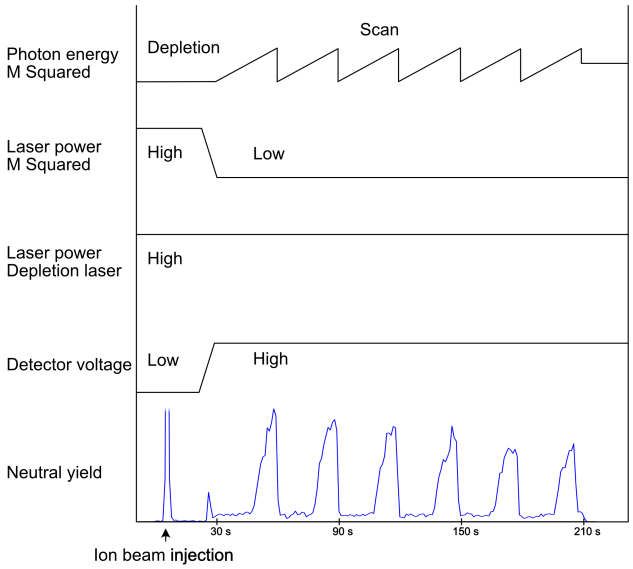

Figure 4.1: Timing of one measurement cycle for the high precision EA measurement of Si.

Table 4.1: Experimentally determined electron affinities for the stable isotopes of Si^- compared to the most recent literature values, where present.

Isotope	EA (eV)	Literature EA (eV)
^{28}Si	1.389 522 01(17)	1.389 521 0(7) [81]
^{29}Si	1.389 521 72(12)	-
^{30}Si	1.389 520 78(12)	-

^{28}Si$^-$

A typical scan of the photon energy over the photodetachment threshold of ^{28}Si$^-$ using the method described above is presented in Figure 4.3. The previous highest precision value for the EA of ^{28}Si is 1.3895210(7) eV [81]. A comparison of the new value for the EA to older measurements is presented in Figure 4.4. Here we can see that the value presented in this work is within 1σ of previous measurements [79, 99, 100], and within 2σ of the the most recent literature value by Chaibi *et al.* [81].

^{29}Si$^-$

In the case of ^{29}Si$^-$, the silylidyne (^{28}SiH$^-$) ion becomes a significant contaminant in the ion beam, due to the relative abundance of the different Si$^-$ isotopes in the ion beam. Unfortunately, the EA of ^{28}SiH$^-$ is 1.277(9) eV [23], which cannot be detached using the depletion laser with a photon energy of 1.178 eV. Instead, to reduce the amount of

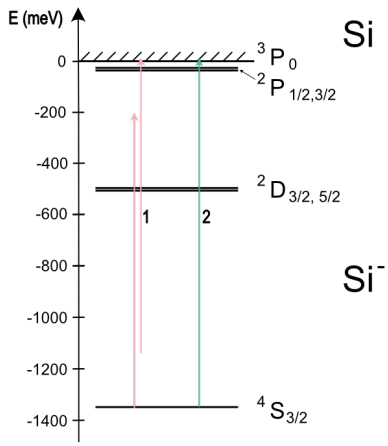

Figure 4.2: The structure of Si$^-$. The two sets of arrows show the laser scheme for the photodetachment procedure. Arrow set 1 shows the first step where the excited states were depleted and arrow 2 shows the photodetachment of the ground state.

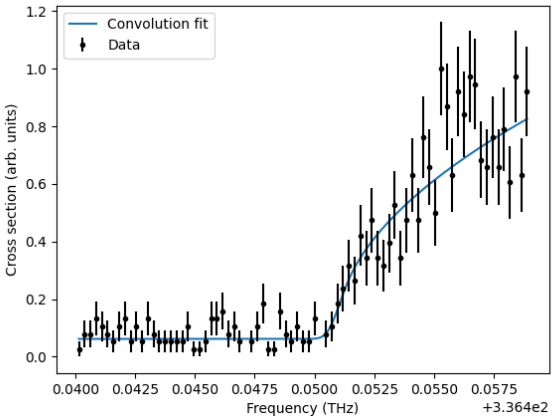

Figure 4.3: Typical scan of the laser frequency over the EA threshold in $^{28}Si^{-}$. This data was obtained in a co-propagating geometry. The solid line is a convolution between the Wigner threshold law and a Gaussian distribution representing the energy spread of the ion beam.

silylidyne in the ion beam, the Ti:Sa laser was set to a high power for 30 seconds, depleting the molecule. The power was then reduced and the laser wavelength was scanned over the ground state threshold of $^{29}Si^{-}$.

On the contrary to the even isotopes, $^{29}Si^{-}$ has a hyperfine splitting in the ground state due to the odd number of nucleons. The ground state has total angular momentum of the electrons, $J = 3/2$, and of the nucleus, $I = 1/2$. This means, according to Equation 2.5, the ground state is split into two states with total angular momentum of the ion, $F = 1$ and $F = 2$.

The EA for ^{29}Si is affected by the hyperfine structure of the ground state of the negative ion and is defined as the energy difference between the lowest hyperfine level, $F = 1$, and the ground state in ^{29}Si. However, in our case it was not possible to resolve the hyperfine splitting in the EA measurements, which means the EA was determined using a one threshold Wigner fit.

The hyperfine structure was investigated by the same methods as the EA and the isotope shifts. To resolve the hyperfine splitting the laser

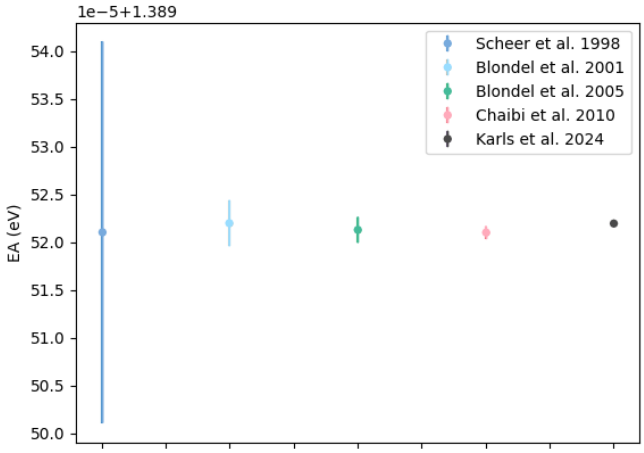

Figure 4.4: The measured EA of ^{28}Si compared to older literature values by Scheer *et al.* [79], Blondel *et al.* in 2001 [99], Blondel *et al.*in 2005 [100] and Chaibi *et al.* [81].

wavelength was scanned repeatedly over a smaller region around the threshold with smaller steps. In this measurement, we are only searching for the separation between two thresholds, and the direction of the laser beam does not affect the results.

A convolution between the Wigner threshold law and a Gaussian distribution was fitted to the data to obtain the values of the two thresholds. The fit was also made without the convolution to more clearly show that the two thresholds can be observed. Typical fits to data from a co-propagating setup are shown in Figure 4.5. The hyperfine splitting was measured to be 1.8(4) μeV.

^{30}Si$^-$

A typical wavelength scan and fit to determine the for the EA for ^{30}Si$^-$ is shown in Figure 4.6.

Isotope shifts

The charge radii $< r^2 >$ of naturally occuring Si$^-$ was measured to be 9.79(2) fm^2 by Schaller *et al.* [101], and electron scattering experiments

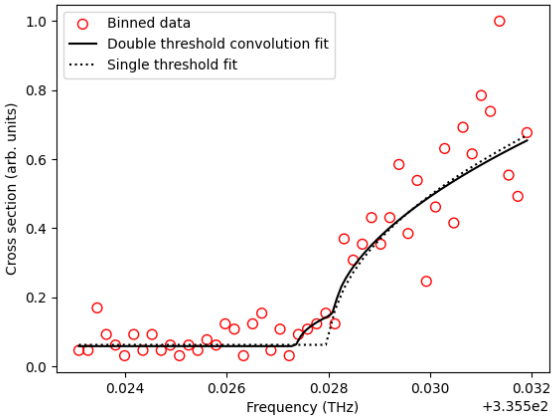

Figure 4.5: Laser frequency scan showing the hyperfine splitting of the ground state in $^{29}Si^{-}$. The solid line represents a convolution between the double threshold Wigner law and a Gaussian distribution representing the energy spread of the ion beam. The dashed line shows a single threshold fit to the same data as a reference. This data was obtained in a co-propagating geometry.

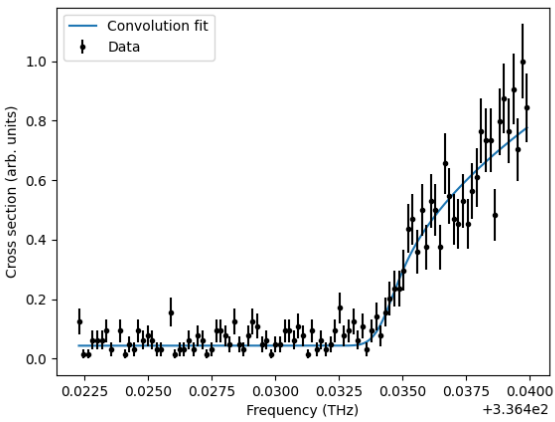

Figure 4.6: Typical scan of the laser frequency over the EA threshold in $^{30}Si^{-}$. This data was obtained in a co-propagating geometry.

Table 4.2: Experimentally determined isotope shifts in the EA for the stable isotopes of Si. The normal mass shift (NMS) was calculated using the experimentally determined EA of ^{28}Si and the specific mass shift (SMS) is the difference between the measured IS and the NMS.

Isotopes	IS (μeV)	NMS (μeV)	SMS (μeV)
$^{29-28}$Si	-0.29(16)	0.9399	-1.23(16)
$^{30-28}$Si	-1.23(16)	1.8151	-3.04(16)

show no indication of change between the different isotopes [71]. This suggests that the field shift would be very small and within the errors of the measured isotope shifts. Thus the specific mass shift can be assumed to be the difference between the total measured isotope shift (IS) and the normal mass shift. The isotope shifts for the different Si isotopes are presented in Table 4.2.

4.1.2 Radioactive isotopes at ISOLDE

^{128}I

EA measurements of radioactive isotopes are special in the sense that the experiments can only be performed at certain radioactive ion beam facilities. The first ever EA measurement of a radioactive isotope was the EA measurement of ^{128}I at ISOLDE using the GANDALPH end-station with a neutral particle detector [77]. A 20 keV $^{128}I^-$ ion beam was overlapped with a laser beam with maximum average power of 450 mW after the interaction region, described in Section 3.2.1. The laser was scanned over the known ^{127}I threshold at approximately 405 nm, and was kept at one wavelength accumulating data for 10 cycles of the PSB before moving on to the next wavelength. These measurements were done in co-propagating geometry and then the Doppler shift was corrected for with the relativistic Doppler shift formula according to Equation 3.2.

To test the GANDALPH setup at ISOLDE, the EA of ^{128}I was measured and compared to the well-characterised EA of stable ^{127}I, measured by Peláez *et al.* 3.059 046 3(38) eV [102]. The resulting EA of ^{128}I was found to be 3.059 052(38) eV. A p-electron is detached, and thus

the threshold has a sharp onset, as this yields an *s*-wave threshold. This means that the EA could be determined with high enough precision to conclude it was in good agreement with the EA of ^{127}I. A fit of the Wigner law to the experimental data can be seen in Figure 4.7. Furthermore, the isotope shift of such a heavy ion is not predicted to be very large, which could also be confirmed when comparing the result with the known EA of ^{127}I. The isotope shift was simply too small for us to resolve. An isotope shift in neutral iodine, ^{127,129}I has previously been measured to $\sim 1\mu$eV by Engleman *et al.* [103]. This isotope shift would again be too small to be resolvable.

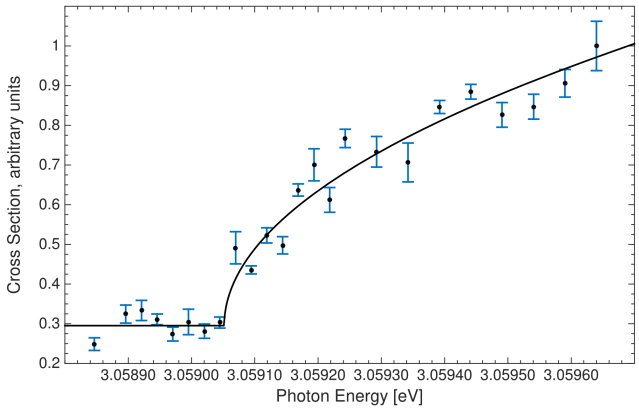

Figure 4.7: Photon energy scan over the EA threshold of ^{128}I and Wigner law *s*-wave fit [77].

^{211}At

Astatine is difficult to produce and is the least abundant naturally occurring element on Earth [38], which means this element had to be synthesised using proton bombardment of a target material as described in section 3.2.1.

The successful production of negative ^{211}At was thus crucial for the experiment to be feasible. This had only been done a few times prior to our experiment, and the resulting yields were large enough to be able to do successful measurements of this elusive species with the GANDALPH detector.

The electron affinity of ^{211}At was measured at ISOLDE using the upgraded version of GANDALPH [86]. The ion beam was overlapped with a laser beam with average power in the range 20–30 mW in the interaction region, described in Section 3.2.1. The scan range was 510 nm–514 nm. Using the improved neutral particle detector, the measurement was performed both in a co- and counter-propagating geometry in order to eliminate the Doppler shift and obtain better precision of the resulting EA. The shift-corrected EA was then calculated using the geometric mean (see Equation 3.1) of the co- and counter-propagating values [104].

The beam current of ^{211}At was typically 600 fA as measured by a Faraday cup immediately before the GANDALPH chamber. After the interaction region, the ion beam was too weak to be measured in a Faraday cup, but the ion count rate could be continuously monitored using a CEM. The transmission of ions through the chamber was estimated to be approximately 1%, which, given an ion velocity of 135,000 m/s, resulting in an average of 0.1 ions in the interaction region.

The EA of ^{211}At was successfully measured to be 2.41578(7) eV. In the case of At^-, the outgoing electron is also an *s*-wave electron and the threshold could thus be determined to a high level of precision, as shown in Figure 4.8. Together with the previously measured ionisation potential (IP) [105], the electronegativity of ^{211}At was determined to be $\chi_M = 5.87$ eV, using the Mulliken electronegativity scale [106].

There were a number of theoretical calculations of the EA of ^{211}At performed prior to our work, but the results of these differ a lot [107–118]. In our work, Borschevsky and co-workers from the Van Swinderen Institute for Particle Physics and Gravity at the University of Groningen, performed state-of-the-art relativistic quantum mechanical calculations, including both Breit and quantum electrodynamics (QED) corrections, and the electron–electron correlation effects. These calculations yielded a value of 2.414(16) eV for the EA, evidently in good agreement with our experimental result of 2.41578(7) eV. The comparison of our experimental value and both Borschevsky's new and other previous calculations are illustrated in Figure 4.9.

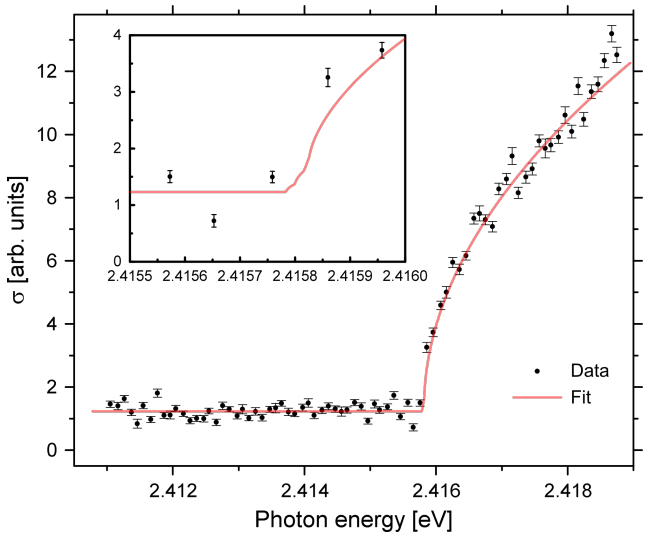

Figure 4.8: Photon energy scan over the EA threshold of ^{211}At and Wigner law s-wave fit to the data (solid line)[85]. The inset shows the threshold, where the different small onsets represent the hyperfine splitting of the ground state in neutral At.

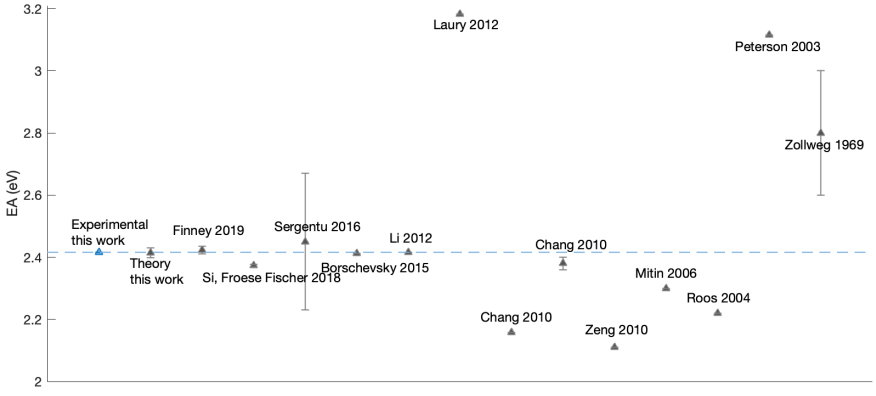

Figure 4.9: Comparison between the measured experimental value of the EA of 211At (dashed line), and both present and historical theoretical calculations [107–118].

4.1.3 Measurements using combined LPTS and RIS at GUNILLA

Alkali anions have closed s-shells, allowing them to be viewed as two-electron systems and this makes systems like the Rb anion potentially highly interesting to study. However, this also means that during photodetachment, the detached electron is an s-electron, causing a p-wave onset of the threshold. As opposed to the sharp s-wave threshold, the p-wave has a slow onset (see Figure 2.2). These thresholds are difficult to measure to a high precision using only LPTS. Thus, the method of photodetachment into an excited state of the neutral atom, followed by photoexcitation into a Rydberg state subsequently accompanied by field ionization can instead be used to observe a sharp onset of the EA threshold with very low background.

The EA for Rb was measured by using LPTS followed by resonance ionization spectroscopy (RIS) to selectively photodetach Rb^- into the $5p^2P_{3/2}$ state and excite to the $37d^2D_{5/2}$ Rydberg state of the neutral Rb atom [97]. This was then followed by field ionization of the neutral atoms. The ionization scheme is shown in Figure 4.10. These measurements were performed using a field ionizer and position sensitive detection spectrometer RADAR, see Figure 4.11, mounted on the GUNILLA beamline as shown in Figure 3.7. When the ions enter RADAR, they are overlapped with two laser beams, separated in time by a few nanoseconds, in the interaction region where the anions are photodetached and excited by the laser beams. The experiment was performed in both a co- and counterpropagating geometry to acount for the Doppler shift. The laser used for the photodetachment of Rb^- was a Sirah Precision Scan dye laser (PRSC-D-18), with Rhodamine B laser dye, producing 0.5 mJ per pulse measured after the RADAR spectrometer. The wavelength was scanned over the photodetachment threshold region. The second laser used to resonantly excite the neutral Rb atoms was an EKSPLA NT342C-10-SH/SF-WW OPO producing 50 μJ per pulse after RADAR. Both lasers were pumped by 10 Hz Nd:YAG pulsed lasers.

Following the interaction with these lasers, the ions enter the region of the field ionizer consisting of four circular ionizer plates. The first and last plates were at ground potential, whereas the two middle plates were set to -629 V and -1224 V, respectively. The potential difference between the second and third plates was large enough to ionize the Rydberg atoms

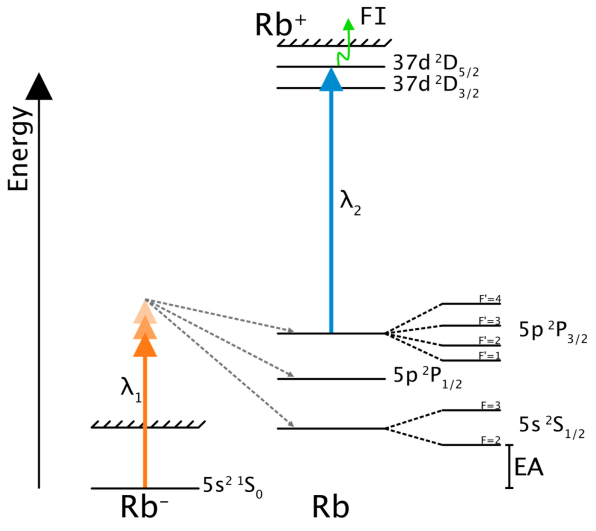

Figure 4.10: An energy level diagram showing some of the energy levels in Rb^- and neutral Rb, and the ionization scheme used for the LPTS and RIS measurements. Figure courtesy of A. Ringvall-Moberg [97].

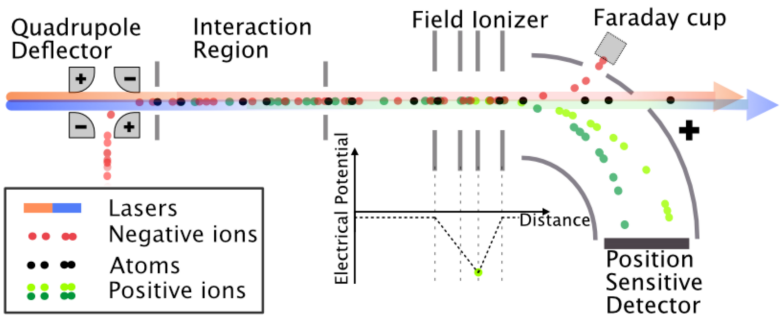

Figure 4.11: The RADAR spectrometer used for the EA measurement for Rb^-. Figure courtesy of A. Ringvall-Moberg.

by the time they pass the third plate. The now positively charged ions were decelerated by over 1 kV due to the potential difference between the last two plates.

After the field ionizer, the lower energy positive ions were deflected with an energy analyzer and detected with a position sensitive detector, consisting of stacked MCPs and a delay line anode, ensuring only field ionized ions were registered as signal. In addition to the field ionized positive ions, there was also a background of positive ions created by ion-ion collisions or laser induced multi photon ionization. The remaining neutral atoms that were not ionized by the field ionizer continue along a straight path, whereas the ions that were still negatively charged were deflected into a Faraday cup. A schematic drawing of RADAR is shown in Figure 4.11.

In addition to the EA measurement, the lifetime of the $5p^2P_{3/2}$ state in neutral Rb was investigated by measuring the yield of positive ions as a function of the time delay between the laser pulses. At GUNILLA, the EA of Rb^- was determined to be 485.898(4) meV, which represents a fivefold improvement in the uncertainty compared to the preexisting value of 485.916(21) meV [119]. The Wigner s-wave threshold law was fitted to the data recorded around the threshold of the ground state in Rb^- according to:

$$\sigma = a + b \sum_{F=1}^{4} (2F+1)(E-(E_{\mathrm{Th}}+E_{\mathrm{hfs,F}}))^{l+1/2}\Theta(E-(E_{\mathrm{Th}}+E_{\mathrm{hfs,F}})), \quad (4.1)$$

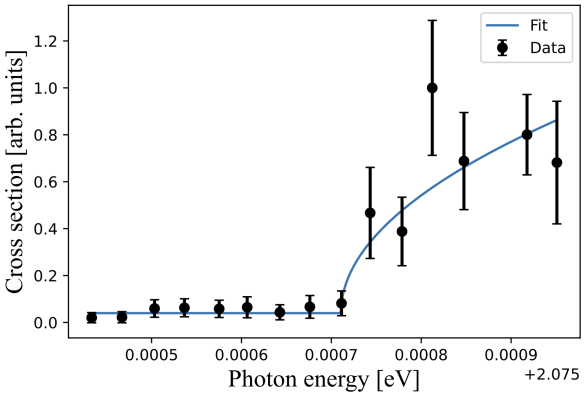

Figure 4.12: A typical threshold scan of the ground state photodetachment threshold in Rb^- into the excited state $5p^2P_{3/2}$ in neutral Rb. The data was recorded in a co-propagating geometry. The solid line represents the Wigner threshold law s-wave fit described in Equation 4.1.

where a and b are constants corresponding to the background and amplitude respectively, E is the photon energy, E_{Th} is the threshold energy, $E_{\mathrm{hfs,F}}$ is the energy corresponding to the hyperfine level F in the $^2P_{3/2}$ state in neutral Rb, l is the angular momentum of the outgoing electron, which in the case of an s-wave is zero, and Θ is the Heaviside step function. A typical photon energy scan over the EA threshold, performed in a co-propagating geometry, and fit of the data are presented in Figure 4.12.

Several measurements were performed with both co- and counter-propagating beams. The threshold energy corrected for the Doppler shift, $E_{\mathrm{Th}}^{\mathrm{Corr}}$, was then extracted by taking the geometric mean value according to Equation 3.1. Thus the resulting EA could be calculated according to

$$E_{EA} = E_{\mathrm{Th}}^{\mathrm{Corr}} - \left(E(^2P_{3/2}) - E(^2S_{1/2})\right), \tag{4.2}$$

where $E(^2P_{3/2}) - E(^2S_{1/2})$ is the well-known energy difference between the ground state and the $^2P_{3/2}$ state in neutral Rb of 1.589049 eV [120].

In addition to the EA, the lifetime of the $^2P_{3/2}$ state in neutral Rb was investigated. This was done by measuring the yield of positive ions as a function of the time delay between the two different laser pulses,

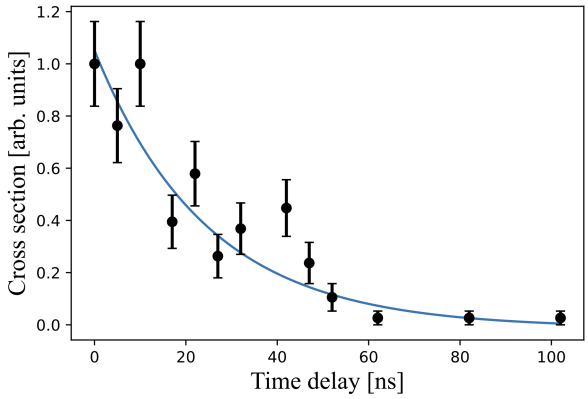

Figure 4.13: Neutral yield as a function of time delay between two laser pulses. Rb^- was photodetached and photoexcited into an excited state in neutral Rb by the first laser and thereafter ionized into Rb^+ by the second laser. Resulting lifetime of the $^2P_{3/2}$ state is 24.3(24) ns.

depicted in Figure 4.13. If anions photodetached by the first laser decay to a lower energy state before being hit by the second excitation laser, they will instead remain neutral and will not be detected. An exponential decay curve was fitted to the data and the extracted lifetime of this excited state is 24.3(24) ns, in agreement with the tabulated value of 26.0(18) ns [121].

4.2 Part II - Lifetime measurements

The second part of this thesis covers lifetime measurements of the excited states in several different atomic and molecular negative ions, presented in Papers VI-XI. These measurements were all performed at DESIREE, where the long storage times allow for investigations of the population dynamics of these metastable states.

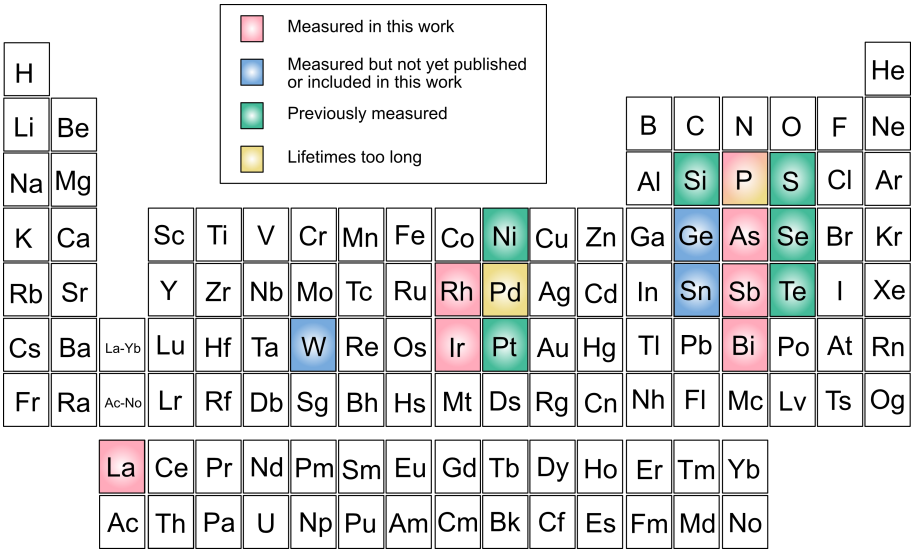

Figure 4.14: Overview of lifetime measurements.

4.2.1 Lifetime measurements at DESIREE

An overview of the different elements for which lifetime measurements were performed is shown in Figure 4.14. The ions were created with a non-thermal distribution in a hot cesium sputter ion source. The ions were typically accelerated to energies of 10 keV. They will decay when interacting with the cryogenic temperatures of the walls of the chamber.

The ions were typically stored in the symmetric ring of DESIREE, where a laser beam intersected the ion beam in either a collinear or crossed beam geometry. The ion currents were typically kept to less than 1 nA in order to reduce the risk of ion-ion collisions, and the laser power was significantly reduced so as to avoid depleting the ions.

The storage time of the total ion beam was measured either by letting the ion beam decay by collisions with the background or by probing all states in the ions with a low power continuous wave (cw) Ti:Sa laser or a pulsed OPO with a photon energy higher than the EA of the studied element. In order to avoid depletion of the ions, the beam was intermittently blocked using a shutter.

The lifetimes of the excited states in negative ions were measured by probing only the state of interest by using an IR laser with sufficient

photon energy to detach the excited state, but not the ground state of the element of interest. If the ion has multiple excited states it can be difficult to determine the lifetime of a specific energy state. However, there are a few different methods that can be used to solve this issue. One approach is to study the separate states on different time scales, if this is applicable. This is very useful if the lifetimes of the different excited states are predicted to differ by at least an order of magnitude. If this is not the case, another technique is to make fits to the data that include multiple exponential decay terms corresponding to the individual states. If the laser can detach only the weakest bound state, the lifetime of this state can be determined first and then locked when analysing the more strongly bound states, which increases the accuracy. Another possibility for extracting the lifetime of an individual state can be if a state with a small population can be disregarded in a measurement, which can be done in case the separate excited states differ significantly in their population. Using one or a combination of these methods it is possible to separate the lifetimes of several excited states.

In both the case of measurements of the total ion beam storage time and the lifetimes of the excited states, the photodetatchment signal was monitored as a function of time and an exponential decay curve was fitted to the data in order to extract the lifetime(s).

Transition metals

The electronic structure of the iridium and rhodium anions have been mapped out, as well as the lifetimes of the excited states in these ions. Energy diagrams showing the ground state and excited state energy levels are shown in Figure 4.15. These measurements were carried out at the symmetric ring at DESIREE.

Further, the structure of Ir^- was investigated and these results agreed with previous measurements and theory [122], but with the additional observation of one previously unknown bound excited state. The energy of the $^3P_2$ state was experimentally determined to have a binding of 1.045(2) eV, which agrees well with the result from the recent study by Y. Lu *et al.* [123]. The binding energy of the previously unobserved $^3P_2 + ^3F_2$ state could be experimentally determined to be < 0.6702 eV.

The experimentally derived lifetimes of all three excited states of Ir^- were compared with theoretical calculations of the same lifetimes,

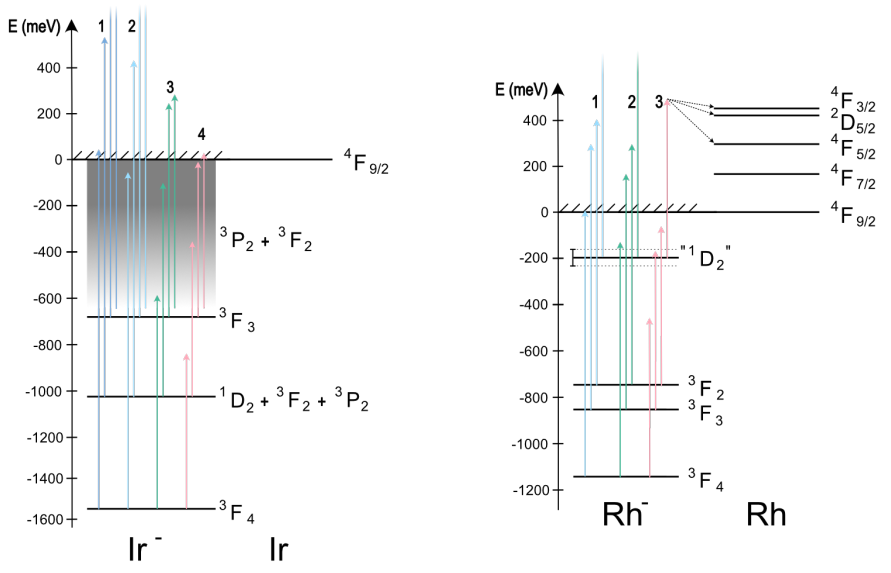

(a) Ir^-. **(b)** Rh^-.

Figure 4.15: Energy level diagrams of Ir^- and Rh^-. Arrow sets 1-4 indicate different photon energies for photodetachment.

as shown in Table 4.4. The experimental values for the lifetimes of all excited states are in good agreement with the theoretically calculated values. In Figure 4.16, the experimental data and resulting lifetime fit of the $^3P_2(47\%) +^3 F_2(42\%)$ state in Ir^- can be seen.

Another transition metal, Rh^-, was also investigated and Figure 4.17 shows the lifetime of a previously unobserved state in Rh^-. The energy of this state was investigated further at the GUNILLA facility at the University of Gothenburg, as described in Section 3.2.3. This experiment was performed in a similar setup to the EA measurements at ISOLDE in Figure 3.4. Negative ions were produced with a cesium sputter ion source and mass selected in a mass selection magnet. The ion beam was then guided through some ion optics and bent 90° to the interaction region where it was overlapped with a laser beam in a co- or counter-propagating setup. The laser wavelength was tuned over the energy threshold and the neutral atoms produced by photodetatchment were detected.

The third excited state is, according to theoretical MCDHF calculations a state of highly mixed $^1D_2 +^3 P_2 + (4d^9 5s)^1 D_2 +^3 F_2$ composition. This energy level is for simplicity labeled "$^1D_2$" from the main contributing term. The photon energy of the OPO laser was scanned over the threshold for this state. However, due to limitations in the laser scan region, it was not possible to determine exactly which transition this corresponds to, but in Table 4.3 the different possibilities are presented. The exact energy of the state cannot be determined, but can be placed in the interval $0.1584(2)\ \text{eV} < E_b < 0.2669(2)\ \text{eV}$.

All energies and lifetimes of Rh^- can be viewed in Table 4.4. The discrepancy between theory and experiment increases for the "$^1D_2$" state, as the theoretically calculated *ab initio* lifetime for this state was found to be $\tau = 1.6(2)$ s, much shorter than the experimentally measured lifetime. Rescaling the lifetime with the experimental energy increases the computed lifetime to the range $2.7(6) - 4.6(9)$ s, closer to the experimental lifetime. The discrepancy in lifetimes for this state shows that we still do not fully understand the nature of this highly mixed excited state.

In addition to the bound excited states, an autodetaching state was also found. The energy of this state could not be determined, but the lifetime was found to be 318(20) μs.

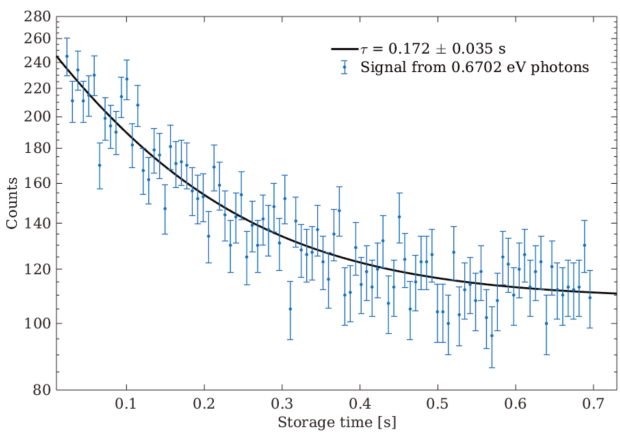

Figure 4.16: Lifetime measurement of the $^3P_2(47\%) +^3 F_2(42\%)$ state in Ir^-, with a resulting lifetime of $\tau = 172(35)$ ms [124].

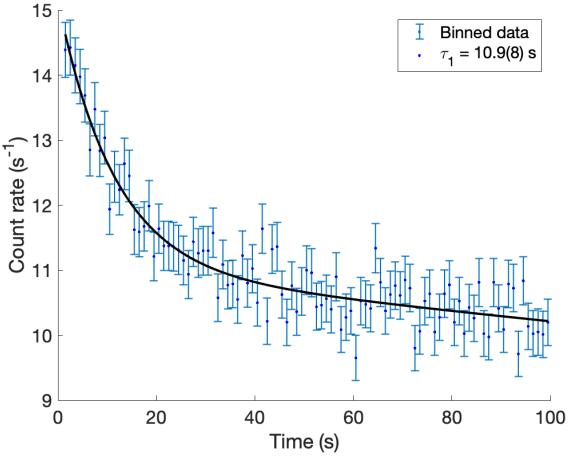

Figure 4.17: Lifetime measurement of the "$^1D_2$" state in Rh^-, with a resulting lifetime of $\tau = 10.9(8)$ s.

Table 4.3: Potential transitions for the "$^1D_2$" threshold Rh^- measured at GUNILLA. The first two transitions should be significantly suppressed due to the large ΔJ and detachment of a d-electron. Thus, we can conclude that the measured threshold is to the $^3F_{5/2}$, $^3F_{3/2}$ or $^2D_{5/2}$ state in Rh I. This results in a binding energy in the interval $0.1584(2)$ eV $< E_b < 0.2669(2)$ eV.

Transition	Rh I E_{exc} (eV)	Res. E_b (eV)
"$^1D_2$" $\rightarrow (4d^8 5s)^3F_{9/2}$	0	0.5890(2)
"$^1D_2$" $\rightarrow (4d^8 5s)^3F_{7/2}$	0.189692	0.3993(2)
"$^1D_2$" $\rightarrow (4d^8 5s)^3F_{5/2}$	0.322115	0.2669(2)
"$^1D_2$" $\rightarrow (4d^8 5s)^3F_{3/2}$	0.430557	0.1584(2)
"$^1D_2$" $\rightarrow (4d^9)^2D_{5/2}$	0.410370	0.1786(2)

Elements in the nitrogen group

The anions of four elements in the nitrogen group have been investigated: P^-, As^-, Sb^- and Bi^-. The energy level diagrams of these elements are presented in Figure 4.18. These measurements were performed in the

Table 4.4: Energy levels and lifetimes of excited states in Ir^- and Rh^-. The binding energies E_b^{th} are theoretically calculated excitation energies using either valence-valence (VV) correlation model or including core-valence (CV) correlation contributions. The theoretical lifetimes are based on the experimentally measured energy levels.

Ir^-

Energy level	E_b^{th} (eV)	E_b^{exp} (eV)	τ_{exp} (s)	τ_{th} (s)
$^3F_4$	-	1.56436(15) [122]	-	-
$^1D_2 + ^3F_2 + ^3P_2$	0.97446^1 0.92730^2	1.045(2)	$> 1200(100)$	> 2500
$^3F_3$	0.73885^1 0.69417^2	0.68635(5) [125]	0.133(10)	0.112(11)
$^3P_2 + ^3F_2$	0.14372^1 0.07858^2	< 0.6702	0.172(35)	0.161(8)

Rh^-

Energy level	E_b^{th} (eV)	E_b^{exp} (eV)	τ_{exp} (s)	τ_{th} (s)
$^3F_4$	-	1.14289(20) [69]	-	-
$^3F_3$	0.868^1 0.856^2	0.849(8) [126]	3.2(6)	2.9(2)
$^3F_2$	0.726^1 0.707^2	0.725(8) [126]	21(4)	20.0(4)
"$^1D_2$"	0.106^1 0.036^2	bound[3]	10.9(8)	2.7(6) [4] $-4.6(9)$
"$^3P_2$"	-0.242^1 -0.324^2	unbound	-	2.3^1 4.7^2

[1] Valence-valence (VV) correlation model.
[2] Including core-valence (CV) correlation contributions.
[3] $0.1584(2)$ eV $< E_b < 0.2669(2)$ eV.
[4] Corresponding to the experimental energy interval $0.1584(2)$ eV $< E_b < 0.2669(2)$ eV.

same way as previously described for the investigated transition metals.

An overview of the results for the measured lifetimes of these elements in the group is displayed in Figure 4.19. These results show that the lifetimes of the excited states in P^- are too long to be measured at DESIREE, in agreement with theoretical calculations [127].

Bi^- has one bound excited state, $^3P_0$. The lifetime measurement of this state is presented in Figure 4.20 [128]. In this particular case, there was a noticeable dependence on the laser power of the measured lifetime of the excited state. The lifetime was therefore measured using several different laser powers and then the resulting lifetime was extracted by extrapolating to zero laser power in a Stern-Volmer plot.

Similar tests were performed also for the other ions in this group, but the vast majority did not seem to be affected to the same extent. Instead, the laser power was chosen to be sufficiently low as not to significantly affect the amount of ions in the storage ring and thus also not affect the measured lifetime.

La^-

La^- is an ion with an unusually large number of bound states of both even and odd parity [65, 129]. The electric dipole transition between the $^3F_2^e$ and $^3D_1^o$ states has been proposed as a cycling transition, making La^- a promising candidate for laser cooling. However, it has been predicted that there could be some leakage out of the nearly closed channel cycle, due the transition into long lived metastable states in the ion, which means re-pumping would be required [66].

At DESIREE, the lifetimes of three metastable states in La^- were measured. The energy level diagram is shown in Figure 4.21. These lifetimes were measured using laser spectroscopy in a crossed beam geometry. The lasers used were a 10 Hz pulsed OPO at 1550 nm for detachment of the ground state $5d^26s^2\ ^3F_2^e$ and all excited states. The same laser at 2230 nm was used to detach ions in the first excited state, $5d^26s^2\ ^3F_3^e$ (and, of course, all other excited states as well). For the $5d^26s^2\ ^3F_4^e$ state, a 2800 nm CW diode laser in collinear geometry was used. At this wavelength, another short-lived excited state, possibly belonging to a $5d6s^26p\ ^1D_2^o$ state, was also detached. The different photon energies used are marked with arrow sets labeled “1”, “2” and “3” in Figure 4.21. The measured lifetimes for the excited states in La^- are

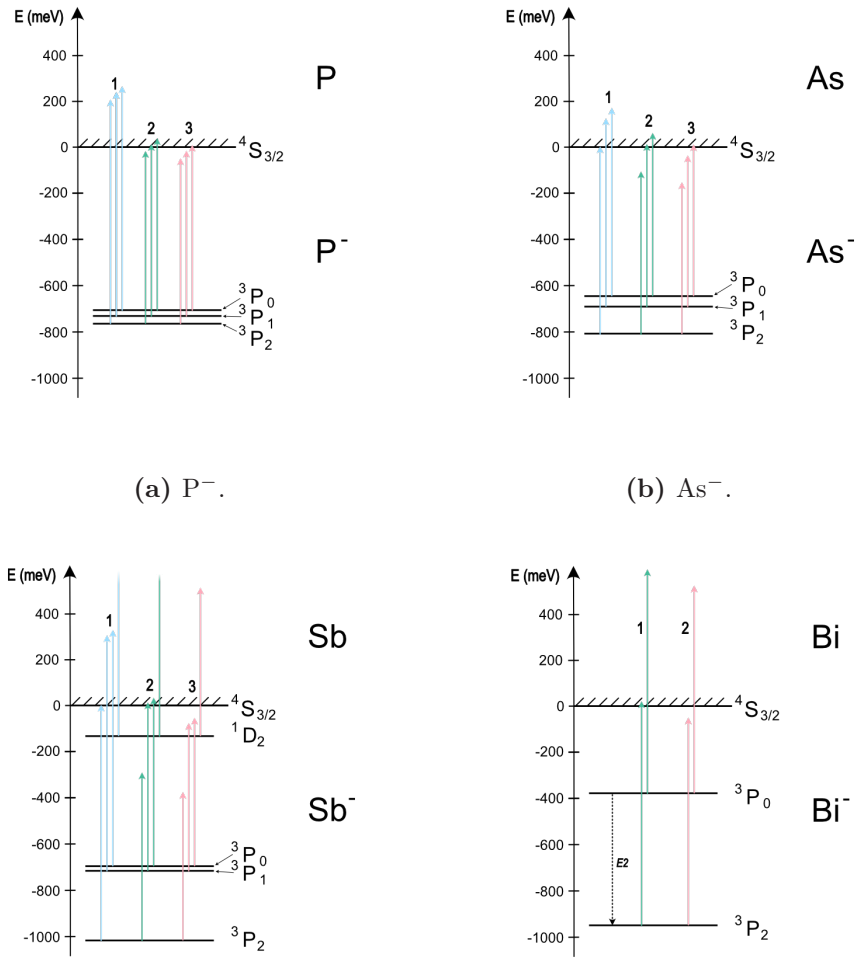

(a) P^-. **(b)** As^-.

(c) Sb^-. **(d)** Bi^-.

Figure 4.18: Energy level diagrams for four elements in the nitrogen group. The arrow sets labeled "1" correspond to detachment of ions in all states, whereas the arrow sets labeled "2" and "3" correspond to detachment of ions in excited states.

presented in Table 4.5. The results show that decays with three different

Table 4.5: Energy levels and lifetimes of the investigated excited states in La^-. τ_{exp} are the experimentally measured lifetimes, whereas τ_{th} represent theoretically calculated values by O'Malley *et al.*

Energy level	E_b (eV)	τ_{exp} (s)	τ_{th} (s)
$^3F_2^e$	0.557546(20) [130]	-	-
$^3F_3^e$	0.473609(36) [131]	132(20)	132 [129]
$^3F_4^e$	0.384664(31) [131]	32(5)	134 [129]
$^1D_2^o$**?**	0.3348(74) [131]	0.22(3)	0.0038[1] [129]

[1] This is the calculated lifetime of the $^1D_2^o$ state. As mentioned in the text, the discrepancy between the measured lifetime and this one is very large, suggesting the measured lifetime could belong to a weaker bound state in La^-.

lifetimes were found, two of which can be assigned to the ^{3}F-states. This lifetime is in excellent agreement with theoretical calculations, whereas the lifetime of the $^3F_4^e$ state was measured to be significantly shorter than theoretical predictions, as shown in Figure 4.22. The third lifetime is significantly shorter than the other two, and is currently unidentified, but it could belong to the decay of the $^1D_2^0$ state. However, the calculated

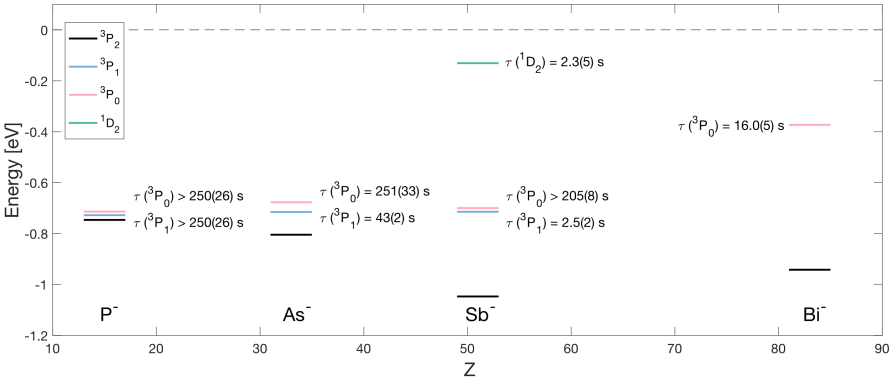

Figure 4.19: An overview of the measured radiative lifetimes in P^-, As^-, Sb^- and Bi^-.

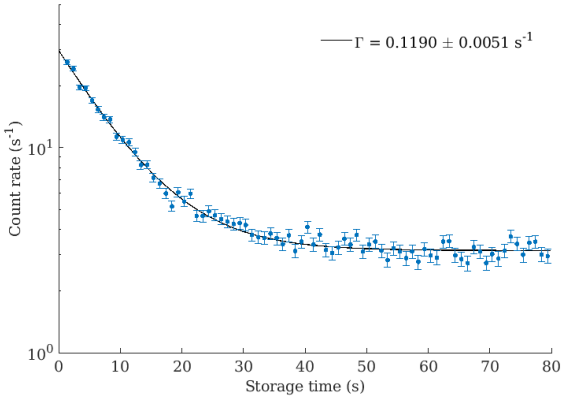

(a) Lifetime measurement and exponential decay fit of the $^3P_0$ excited state in Bi^-.

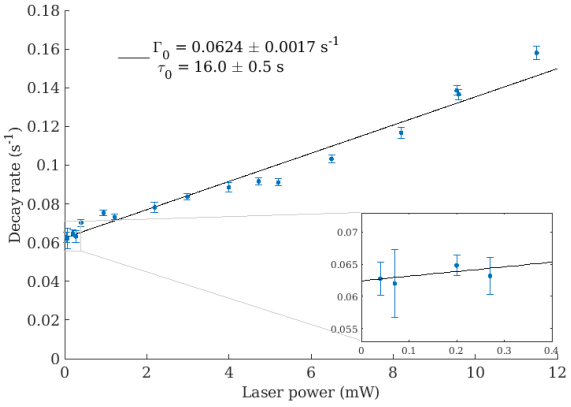

(b) Decay rates of Bi^-.

Figure 4.20: Bi^- results [128].

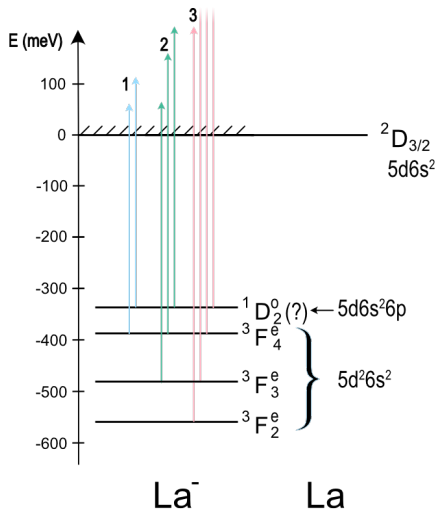

Figure 4.21: The energy levels of La^- studied in this work, with the photon energies corresponding to three different detachment modes marked with arrow sets. Arrow set 1 corresponds to a wavelength of 2800 nm, only detaching the $^3F_4^e$ and $^1D_2^o$ states. Arrow set 2 corresponds to a wavelength of 2230 nm and detaches $^3F_3^e$ as well. Arrow set 3 represents a laser of the wavelength 1550 nm, which will detach all states.

lifetime of this state is 0.0038 [129], roughly 50 times shorter than the measured lifetime. Thus, it could belong to any of the other, more weakly bound, excited states in La^-.

The lifetimes of both the $^3F_4^e$ and the short-lived state were found to exhibit a relatively strong laser power dependency. Due to this fact, several lifetime measurements were performed at different powers, whereupon the decay rate was taken by extrapolating the decay rate to zero laser power.

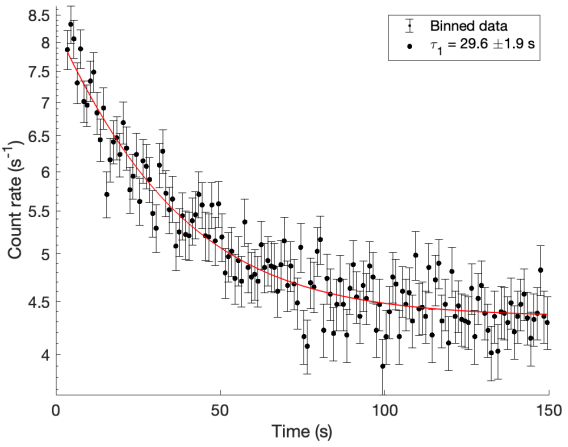

(a) One of the measurements showing the decay of the $^3F_4^e$ state in La $^-$. The lifetime of this state proved to be dependent of the laser power, and thus several measurements were performed at different laser powers.

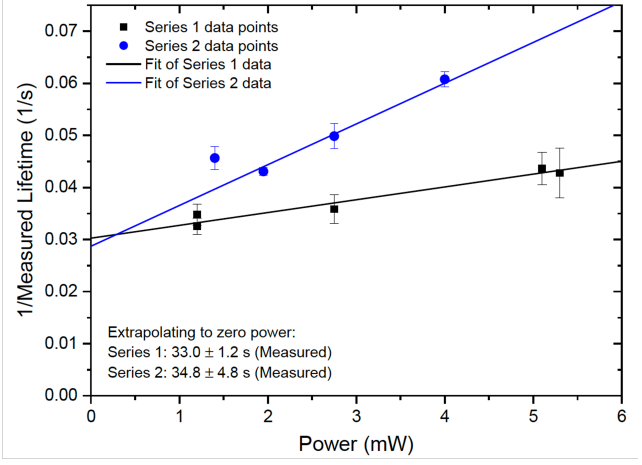

(b) Plot showing the laser power dependence for the lifetime of the $^3F_4^e$ state in La$^-$. The lifetime at zero laser power was extracted as the lifetime of the state. Two series of measurements were recorded, yielding a τ at zero laser power of 32(5) s.

Figure 4.22: Decay of the $^3F_4^e$ state in La$^-$[132].

WF_5^- and HfF_5^-

With the possibility of storing ion beams for longer periods of time, measurements of the decaying excited states can of course also be performed on molecules. In astrophysics, the abundance of ^{182}Hf in stellar environments plays an important role in understanding of the nucleosynthesis of heavy elements. ^{182}Hf is unstable and decays into ^{182}W via the two-step β^--decay:

$$\begin{aligned} {}^{182}_{72}\mathrm{Hf} &\rightarrow {}^{182}_{73}\mathrm{Ta} + e^- + \bar{\nu}_e \\ {}^{182}_{73}\mathrm{Ta} &\rightarrow {}^{182}_{74}\mathrm{W} + e^- + \bar{\nu}_e, \end{aligned} \tag{4.3}$$

where the first decay has a half-life of $8.9 \cdot 10^6$ years compared to the second decay with a half-life of 114 days, making the ^{182}Ta intermediate nuclide negligible. Thus, the relationship between the ^{182}W and ^{182}Hf abundance is of particular interest due to its use as a chronometer for geochronological radiometric dating. The relative abundance of these two elements give information about the evolution in the early universe. There is a large interest in studying the natural abundances of ^{182}Hf using accelerator mass spectrometry (AMS) [133]. However, the large background of ^{182}W makes this difficult. Photodetachment of the interfering ion was investigated as a method of suppressing this large background. At DESIREE, ion beam storage time measurements and photodetachment studies of the molecules WF_5^- and HfF_5^- were performed. Attempts to measure the EAs of WF_5^- and HfF_5^- were made and spontaneous decays were investigated.

The ions were created in the cesium sputter ion source at DESIREE and populate a large distribution of rotationally and vibrationally excited states. $^{180}HfF_5^-$, and the isotopologues $^{184}WF_5^-$ and $^{186}WF_5^-$ were used in the measurements. The cathodes were made from HfF_4–W–PbF_2 for the WF_5 measurements and HfF_4–PbF_2 for the HfF_5 measurements. The molecular ions were accelerated to 10 keV energies and guided into the symmetric storage ring. The ions were then neutralized by either laser photodetachment or spontaneous decay processes. For the photodetachment measurements, the ion beam was intersected with a 1 kHz pulsed OPO laser in a crossed beam geometry, which was tuned over the wavelength region 240 to 450 nm. The neutral atoms were detected with an imaging detector (ID), consisting of three stacked MCPs and a phosphor screen, which was in turn monitored by a photomultiplier tube.

In the spontaneous decay experiment, the ions can decay either via autodetachment, dissociation or radiative cooling. The processes can be described by

$$(WF_5^-)^* \rightarrow WF_5 + e^-, \tag{4.4}$$
$$(WF_5^-)^* \rightarrow WF_4 + F^-, \tag{4.5}$$
$$(WF_5^-)^* \rightarrow WF_5^- + h\nu, \tag{4.6}$$

recpectively. Equation 4.4 describes the autodetachement process, Equation 4.5 describes one of the possible dissociation processes and Equation 4.6 describes the radiative cooling process. In these equations, $*$ denotes an excited state, e^- corresponds to the detached electron and $h\nu$ is the energy of the emitted photon. Analogous processes also occur in the HfF_5^- ions.

The spontaneous decay of the molecular ions HfF_5^- and WF_5^- were measured and compared to each other. The resulting lifetime of WF_5^- was found to be $\tau = 2.8(2)$ ms, compared to the somewhat longer HfF_5^- lifetime of $\tau = 12(1)$ ms. This result shows that the spontaneous decay of the WF_5^- ion is about one order of magnitude faster than for HfF_5^-. These two results can be viewed in Figure 4.23. The LPT measurements

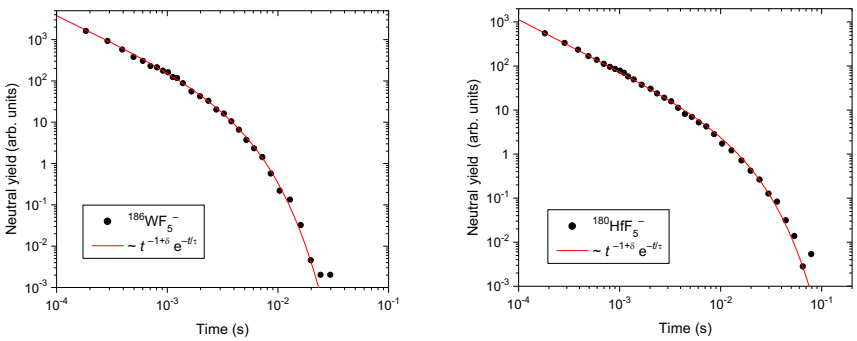

(a) WF_5^-. **(b)** HfF_5^-.

Figure 4.23: Spontaneous decays of WF_5^- and HfF_5^-. Figure courtesy of H. Gnaser [134].

of WF_5 suggests a vertical detachment energy (VDE) of 3.5 eV, which is

slightly lower than the predicted theoretical value of 3.9 eV [135]. On the contrary, the VDE for HfF_5 is still in agreement with the theoretical value of 8.8 eV [135]. The available photon energies at DESIREE go up to ~ 5.2 eV, which was concluded to be too low for photoinduced detachment of HfF_5, as the neutral yield remains significantly low. This means the VDE for HfF_5 must be > 5.2 eV. A plot of the neutral yield of WF_5 ions as a function of photon energy is depicted in Figure 4.24. In this measurement there are too few data points below the threshold to make a reliable Wigner threshold law fit.

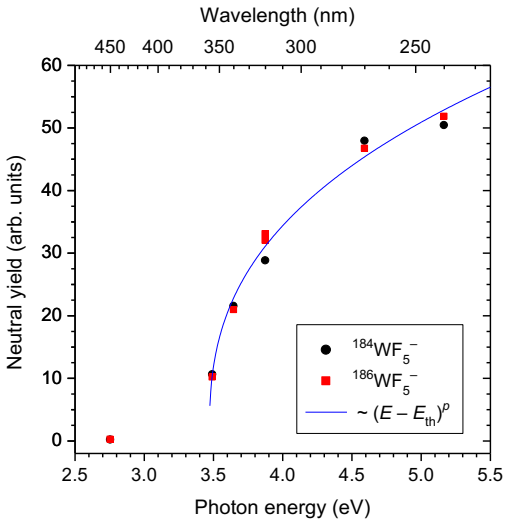

Figure 4.24: WF_5^- threshold. Figure courtesy of H. Gnaser [134].

Chapter 5

Conclusion and outlook

Neutral atomic systems are very well studied, but the corresponding negative systems are significantly less explored. The work in this thesis investigates several properties of negative ions and can be divided into two different parts: the EA measurements of stable and radioactive isotopes and lifetime measurements of excited states in negative ions.

The method of laser manipulation of the quantum levels of the ions, leaving the ions in the ground state, was used to measure the EA and isotope shifts in the Si isotopes. Only a few elements have had isotope shifts investigated, this method opens up for higher precision measurements and thus facilitate investigation of isotope shifts.

This method can also be applied to other types of measurements, i.e. mutual neutralization experiments. In this way, the quantum state of the ion can be known before the mutual neutralization process. This has already been tested at DESIREE for Si^-/Na^+, where the excited states in Si^- were depleted allowing the mutual neutralization process to be limited to the Si^- ions in the ground state. In this experiment, we could clearly see a difference between the manipulated quantum level MN and the same process with Si^- with an estimated population of 3% in the excited ^{2}D states. The results for this experiment are displayed in Figure 5.1, where it is clear that the peak corresponding to the yield of neutral pairs at a separation of $r \approx 25$ mm is significantly reduced for the quantum selective MN process, as compared to leaving the Si^- in all states. However, the peak has not completely vanished, which could imply

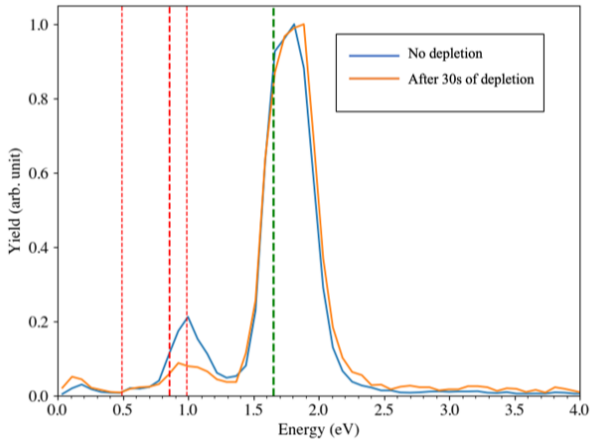

Figure 5.1: Results from the mutual neutralization of Si^-/Na^+ with manipulated quantum levels. The Blur curve represents MN with Si^- in lift unmanipulated and the orange curve represents MN with Si^- in the ground state. The peak at ~ 1 eV does not completely disappear after 30 s of laser depletion of excited states in Si^-. Figure courtesy of R. Poulose.

that there could be contributions from the three fine-structure levels of the metastable state $2p^5 3s^3P$ s in Na^+, which in the MN process could responsible for a similar energy release, responsible for the remaining small peak. A new experiment is therefore planned, where the same MN process will be repeated but for the Si^-/K^+ system to avoid the contribution from metastable states in the cation. The structure of K^+ is very simple, and it does not have any metastable states that could interfere as is the case for Na^+.

In the context of radioactive ions, the EA of ^{128}I and ^{211}At were both successfully measured. In the case of ^{128}I, the result was in good agreement with the EA of ^{127}I [102].

The experimental value for the EA of At is helpful in order to benchmark theoretical calculation methods, since the previous theoretical calculations have shown various results [108–110, 113, 136], and being able to measure this quantity for other purely radioactive elements could test the models further. With the results from the ^{128}I and ^{211}At measurements, we have demonstrated that we now have a possibility to do

LPT measurements on purely radioactive elements. This opens up a whole new field of experiments, in which photodetachment studies of radioactive isotopes, particularly heavier elements with no stable isotopes, can be performed. This means that important chemical properties, such as the electronegativity, can be experimentally determined for these elements for the first time. The isotope of interest in this experiment, ^{211}At, also has important medical applications in targeted alpha therapy (TAT). In addition to these advances, isotope shifts of lighter elements can also be studied using this setup, which means a lot of work exploring exciting fundamental physics can be done. Beamtimes that will measure the EA of Po and isotope shifts in Cl have been obtained. Another advantage of this setup is that it is movable, which means that it can be moved to other radioactive ion beam facilities. This opens up opportunities for the setup to be utilised at more beam time, even during a long shut down at CERN.

At GUNILLA, the electron affinity of Rb was measured to a high precision using LPT in combination with resonance ionization. Using this technique, in combination with the GANDALPH chamber, the possibility of measuring the EA of Fr opens up. Fr is expected to be the second least electronegative element (after Cs), and it is the second least abundant naturally occurring element (after At). It is also the heaviest alkali metal and very unstable. Fr^+ is produced in very large amounts at ISOLDE and with the addition of GANDALPH to the Collinear Resonance Ionization Spectroscopy (CRIS) experiment, it will be possible for the EA of the extremely rare Fr^- to be investigated. In fact, attaching GANDALPH to the CRIS beamline at ISOLDE will facilitate EA measurements of several radioactive isotopes.

The second part of this thesis concerns the lifetime measurements of excited states in negative ions. The advantage of doing experiments at a facility like DESIREE is that ions can be stored for a long time because of the extremely high vacuum and the cryogenic temperatures of the apparatus, resulting in minimal ion losses due to collisions. This means that ions with long lifetimes and weakly populated states can be investigated.

Two of the elements covered in this work are Ir^- and Rh^-. Looking at the lifetimes of a group separate from the oxygen group, which has previously been thoroughly studied, is interesting, since both Ir and Rh are transition metals and have different atomic properties than the

more straight forward oxygen group. The systematic study of elements from different groups in the periodic table could be used to benchmark theoretical calculation methods for negative ions. A few elements in the nitrogen group have also had their lifetimes investigated at DESIREE, and these elements have all had their lifetimes theoretically calculated in a paper by Su *et al.*, and we could see some discrepancies between theory and experiment in some more complex cases. The experimental results could therefore inspire to more comprehensive theoretical models, as these negative ions are significant for studying electron correlation. In the long run we hope to be able to map out the lifetimes of negative ion excited states of the whole periodic table.

Laser cooling of negative ions is a fascinating field of study because of its possible applications in sympathetic cooling of antiprotons. A promising candidate for laser cooling is La^-, whose dynamic properties have been investigated in this work. La^- is a very interesting ion, due to its many excited states with both odd and even parity, and thus another round of more comprehensive calculations for this ion could be worthwhile. The decay of a short-lived state in La^- could clearly be observed, but the energy state this decay belongs to remains unidentified. However, it has been suggested that it could belong to the $^1D_2^o$ state, as this is the most strongly bound odd state in La^- [137]. The measured lifetime of the $^3F_3^e$ state is in good agreement with the theoretical calculations, while the lifetime of $^3F_4^e$ was measured to be around $\frac{1}{4}$ of the theoretical value. Here, just as in the case for Rh^-, the discrepancy between theory and experiment clearly shows that theoretical models are not comprehensive enough when it comes to the case of some negative ions.

Most of the work covered in this thesis involves atomic negative ions. However, some studies of the more complex field of molecular anions have also been performed, where structural and dynamical properties of the WF_5 and HfF_5 anions have been investigated. The results of the photoinduced reaction of the molecular anions WF_5 and HfF_5 show that photodetachment of WF_5 can be done at lower energies than for HfF_5. Thus, this could be used to suppress the amount of WF_5 in the ion beam at AMS facilities, which will facilitate HfF_5 studies. Effective suppression of the WF_5 contaminant in the ion beam, using photon energies of > 3.5 eV, could facilitate easier detection of ^{182}Hf in terrestrial samples and these studies could tell us a lot about Earth's history and the formation of the solar system, as well as about recent cosmic events in or near the

solar system.

In this thesis, both the structure and dynamics of negative ions have been investigated. Observing these two very different properties of the ions can be useful from a theoretical point of view, since the complexity of theoretical models increases significantly for negatively charged systems, as compared to neutral or positively charged systems. A more robust validation of theoretical models is achievable if it is possible to show that both structural and dynamical calculations agree with experimental results. Thus, the results of combined EA and lifetime measurements can be used to benchmark theoretical models. Furthermore, the results in the first part of this work open up the possibility for EA measurements of radioactive isotopes. This means that fundamental chemical properties, such as electronegativity, for elements lacking stable isotopes can be experimentally determined for the first time. These new heavy elements are of fundamental interest from an atomic physics point of view, but the result may even have implications in applications far beyond the field of physics.

.

Acknowledgements

I owe my gratitude to a wide circle of people who supported me in various essential ways. First and foremost, I would like to express my deepest appreciation to my supervisor Dag Hanstorp for all the support and for giving me a chance not only once but twice.

I wish to express my sincere thanks to my examiner Alexandre Dmitriev for his insightful feedback and guidance throughout this process.

My deepest gratitude goes to Di Lu for all the help in the lab and being the best office mate. Without him half of my experiments would not have been possible to pursue.

I would like to extend my sincere thanks to Moa Kristiansson, Paul Martini, José Navarro Navarrete, Henning Schmidt and the DESIREE team for all the hard work and assistance, and for making it possible to run experiments even when I could not be physically present in Stockholm. Special thanks should also go to David Leimbach.

I am deeply thankful to Wesley Walter and Dan Gibson for their collaboration, encouragement, and for the interesting discussions leading to successful experiments. Also thank you to Robin Golser and the other collaborators from Vienna.

I am very grateful to Sebastian Rothe who has been very encouraging, innovative, and helpful, and to the RILIS team for all the help and support during my time at CERN. I also thank the GANDALPH team for the extensive work with negative ions at ISOLDE.

I had the great pleasure of working with Annie Ringvall-Moberg both at CERN and in Gothenburg and I am grateful for all the emergency coffee runs, cups of ice, and for all the fun we have had in the last few

years.

I would like to acknowledge the assistance of Jan-Åke Wiman, who manufactured many of the components used in my experiments in his workshop and I gratefully acknowledge the assistance of level 8 physics team members. My colleagues Miranda Nichols, Ilse Kardasch, Jakob Welander and all the other level 8 physics team members are acknowledged for all the help and support. Thanks especially to Måns Wallner, my fellow thesis-writing colleague.

Special thanks to Richard Squibb both for assistance with chemicals and for proofreading this thesis and helping me improve my writing.

Gratitude is due to my colleagues on the theory side, Jon Grumer and Tomas Brage, whose assistance was crucial in my experiments and research. They have also been helpful and patient in guiding me through theoretical calculations.

I also wish to thank my family for all the support; Christina for the countless hours of babysitting, allowing me to get my work done, Theodor and Arvid, for always being the sunshine in my life.

Last but not least, I would like to express my endless love and gratitude to Felix for his understanding, unwavering patience, and encouragement when it was most needed. This thesis is dedicated to you. You are my person!

Bibliography

[1] E. Rutherford. LXXIX. The scattering of α and β particles by matter and the structure of the atom . *The London, Edinburgh, and Dublin Philosophical Magazine and Journal of Science*, 21(125):669–688, 5 1911.

[2] N. Bohr. I. On the constitution of atoms and molecules. *The London, Edinburgh, and Dublin Philosophical Magazine and Journal of Science*, 26(151):1–25, 7 1913.

[3] N. Bohr. XXXVII. On the constitution of atoms and molecules. *The London, Edinburgh, and Dublin Philosophical Magazine and Journal of Science*, 26(153):476–502, 9 1913.

[4] N. Bohr. LXXIII. On the constitution of atoms and molecules. *The London, Edinburgh, and Dublin Philosophical Magazine and Journal of Science*, 26(155):857–875, 11 1913.

[5] Max Planck. Ueber das Gesetz der Energieverteilung im Normalspectrum. *Annalen der Physik*, 309(3):553–563, 1 1901.

[6] A. Einstein. Über einen die Erzeugung und Verwandlung des Lichtes betreffenden heuristischen Gesichtspunkt. *Annalen der Physik*, 322(6):132–148, 1905.

[7] L. de Broglie. *Recherches sur la théorie des quanta*. PhD thesis, Université de Paris, 1924.

[8] Heisenberg W. Über den anschaulichen Inhalt der quantentheoretischen Kinematik und Mechanik. *Physik*, 43:172–198, 1927.

[9] E. Schrödinger. An Undulatory Theory of the Mechanics of Atoms and Molecules. *Physical Review*, 28(6):1049–1070, 12 1926.

[10] P. A. M. Dirac. The Quantum Theory of the Electron. In *Roy. Soc. Proc., A*, volume 43, pages 610–624, 1928.

[11] J. J. Thomson. Bakerian Lecture: Rays of positive electricity. *Proceedings of the Royal Society A: Mathematical, Physical and Engineering Sciences*, 89:1–20, 1913.

[12] R Wildt. Negative ions of hydrogen and the opacity of stellar atmospheres. *The Astrophysical Journal*, 90:611–620, 1939.

[13] Lewis M. Branscomb and Stephen J. Smith. Experimental Cross Section for Photodetachment of Electrons from H^- and D^-. *Physical Review*, 98(4):1028–1034, 1955.

[14] Lewis M. Branscomb and Stephen J. Smith. Electron Affinity of Atomic Oxygen. *Physical Review*, 98(4):1127–1128, 1955.

[15] H.S.W. Massey. Negative Ions. Cambridge University Press, 1976.

[16] David J Pegg. Structure and dynamics of negative ions. *Reports on Progress in Physics*, 67(6):857–905, 6 2004.

[17] T. Andersen. Atomic negative ions: Structure, dynamics and collisions. *Physics Reports*, 394(4-5):157–313, 5 2004.

[18] R Middleton. *A Negative-Ion Cookbook*. Pennsylvania, 2 1990.

[19] E. Roueff and E. Herbst. Molecular ions in astrophysics. *J. Phys.: Conf. Ser*, 192:12008, 2009.

[20] T Best, R Otto, S Trippel, P Hlavenka, A Von Zastrow, S Eisenbach, S Jézouin, R Wester, E Vigren, M Hamberg, and W D Geppert. Absolute photodetachment cross-section measurements for hydrocarbon chain anions. *The Astrophysical Journal*, 742(6pp):63, 2011.

[21] J Deiglmayr, M Repp, O Dulieu, R Wester, and M Weidemüller. Population redistribution in optically trapped polar molecules. *Eur. Phys. J. D*, 65:99–104, 2011.

[22] M. C. McCarthy, C. A. Gottlieb, H. Gupta, and P. Thaddeus. Laboratory and Astronomical Identification of the Negative Molecular Ion C_6H^-. *The Astrophysical Journal*, 652(2):L141–L144, 12 2006.

[23] Jonathan C. Rienstra-Kiracofe, Gregory S. Tschumper, Henry F. Schaefer, Sreela Nandi, and G. Barney Ellison. Atomic and molecular electron affinities: Photoelectron experiments and theoretical computations. *Chemical Reviews*, 102(1):231–282, 1 2002.

[24] D R Hartree and W Hartree. Self-consistent field, with exchange, for beryllium. *Proceedings of the Royal Society of London. Series A - Mathematical and Physical Sciences*, 150(869):9–33, 5 1935.

[25] L. M. Blau, R. Novick, and D. Weinflash. Lifetimes and Fine Structure of the Metastable Autoionizing $(1s2s2p)^4P_J$ States of the Negative Helium Ion. *Physical Review Letters*, 24(23):1268–1272, 6 1970.

[26] Pontus Andersson, Karin Fritioff, Joakim Sandström, Gerard Collins, Dag Hanstorp, Anna Ellmann, Peter Schef, Peter Lundin, Sven Mannervik, Peder Royen, K. Charlotte Froese Fischer, Fabian Österdahl, Danijela Rostohar, David J. Pegg, N. D. Gibson, Håkan Danared, and Anders Källberg. Radiative lifetimes of metastable states of negative ions. *Physical Review A - Atomic, Molecular, and Optical Physics*, 73(3), 2006.

[27] A. Ellmann, P. Schef, P. Lundin, P. Royen, S. Mannervik, K. Fritioff, P. Andersson, D. Hanstorp, F. C. Fischer, F. Österdahl, D. J. Pegg, N. D. Gibson, H. Danared, and A. Källberg. Radiative lifetime of a bound excited state of Te^-. *Physical Review Letters*, 92(25 I), 6 2004.

[28] E. Bäckström, D. Hanstorp, O. M. Hole, M. Kaminska, R. F. Nascimento, M. Blom, M. Björkhage, A. Källberg, P. Löfgren, P. Reinhed, S. Rosén, A. Simonsson, R. D. Thomas, S. Mannervik, H. T. Schmidt, and H. Cederquist. Storing keV Negative Ions

for an Hour: The Lifetime of the Metastable $^2P^o_{1/2}$ level in $^{32}S^-$. *Physical Review Letters*, 114(14), 4 2015.

[29] H. Becquerel. Sur les radiations invisibles émises par les corps phosphorescents. *Compt. Rend. Hebd. Seances Acad. Sci.*, 501(122), 1896.

[30] W. C. Röntgen. On a New Kind of Rays. *Science*, 3(59), 1896.

[31] P Curie and M Curie. Sur une substance nouvelle radio-active, contenue dans la pechblende. *Comptes Rendus*, 127:175–178, 1898.

[32] Erich Kugler. The ISOLDE facility. *Hyperfine Interactions*, 129, 2000.

[33] J. Dilling, R. Krücken, and G. Ball. ISAC overview. *Hyperfine Interactions*, 225(1-3):1–8, 1 2014.

[34] S. Gales. SPIRAL2 at GANIL: Next Generation of ISOL Facility for Intense Secondary Radioactive Ion Beams. *Nuclear Physics A*, 834(1-4):717c–723c, 3 2010.

[35] Young Seung Kim and Martin W. Brechbiel. An overview of targeted alpha therapy. *Tumor Biology*, 33(3):573–590, 6 2012.

[36] Sture Lindegren, Per Albertsson, Tom Bäck, Holger Jensen, Stig Palm, and Emma Aneheim. Realizing Clinical Trials with Astatine-211: The Chemistry Infrastructure. *Cancer biotherapy & radiopharmaceuticals*, 35(6):425–436, 8 2020.

[37] Per Albertsson, Tom Bäck, Karin Bergmark, Andreas Hallqvist, Mia Johansson, Emma Aneheim, Sture Lindegren, Chiara Timperanza, Knut Smerud, and Stig Palm. Astatine-211 based radionuclide therapy: Current clinical trial landscape. *Frontiers in Medicine*, 9, 2023.

[38] Isaac Asimov. The natural occurrence of short-lived radioisotopes. *Journal of chemical education*, 30(12):616–618, 1953.

[39] B. Thornton and S Burdette. Three more unsung women - astatine discovery. *Nature*, 567(311), 2019.

[40] D. R. Corson, K. R. MacKenzie, and E. Segrè. Artificially Radioactive Element 85. *Physical Review*, 58(8):672–678, 10 1940.

[41] François Guérard, Jean François Gestin, and Martin W. Brechbiel. Production of [^{211}At]-astatinated radiopharmaceuticals and applications in targeted α-particle therapy. *Cancer Biotherapy and Radiopharmaceuticals*, 28(1):1–20, 1 2013.

[42] Vernon T. Davis, Jeffery Thompson, and Aaron Covington. Laser photodetachment electron spectroscopy studies of heavy atomic anions. In *Nuclear Instruments and Methods in Physics Research, Section B: Beam Interactions with Materials and Atoms*, volume 241, pages 118–124, 12 2005.

[43] Dag Hanstorp. An ion beam apparatus for collinear photodetachment experiments. *Nuclear Instruments and Methods in Physics Research B*, 100(5):165–182, 1995.

[44] Christophe Blondel, Christian Delsart, and François Dulieu. The Photodetachment Microscope. *Physical Review Letters*, 77(18):3755–3758, 10 1996.

[45] E. K. Anderson, C. J. Baker, W. Bertsche, N. M. Bhatt, G. Bonomi, A. Capra, I. Carli, C. L. Cesar, M. Charlton, A. Christensen, R. Collister, A. Cridland Mathad, D. Duque Quiceno, S. Eriksson, A. Evans, N. Evetts, S. Fabbri, J. Fajans, A. Ferwerda, T. Friesen, M. C. Fujiwara, D. R. Gill, L. M. Golino, M. B. Gomes Gonçalves, P. Grandemange, P. Granum, J. S. Hangst, M. E. Hayden, D. Hodgkinson, E. D. Hunter, C. A. Isaac, A. J.U. Jimenez, M. A. Johnson, J. M. Jones, S. A. Jones, S. Jonsell, A. Khramov, N. Madsen, L. Martin, N. Massacret, D. Maxwell, J. T.K. McKenna, S. Menary, T. Momose, M. Mostamand, P. S. Mullan, J. Nauta, K. Olchanski, A. N. Oliveira, J. Peszka, A. Powell, C. Rasmussen, F. Robicheaux, R. L. Sacramento, M. Sameed, E. Sarid, J. Schoonwater, D. M. Silveira, J. Singh, G. Smith, C. So, S. Stracka, G. Stutter, T. D. Tharp, K. A. Thompson, R. I. Thompson, E. Thorpe-Woods, C. Torkzaban, M. Urioni, P. Woosaree, and J. S. Wurtele. Observation of the effect of gravity on the motion of antimatter. *Nature*, 621(7980):716–722, 9 2023.

[46] D Zajfman, A Wolf, D Schwalm, D A Orlov, M Grieser, R von Hahn, C P Welsch, J R Crespo Lopez-Urrutia, C D Schröter, X Urbain, and J Ullrich. Physics with colder molecular ions: The Heidelberg Cryogenic Storage Ring CSR. *Journal of Physics: Conference Series*, 4:296–299, 1 2005.

[47] R. Von Hahn, F. Berg, K. Blaum, J. R. Crespo Lopez-Urrutia, F. Fellenberger, M. Froese, M. Grieser, C. Krantz, K. U. Kühnel, M. Lange, S. Menk, F. Laux, D. A. Orlov, R. Repnow, C. D. Schröter, A. Shornikov, T. Sieber, J. Ullrich, A. Wolf, M. Rappaport, and D. Zajfman. The electrostatic Cryogenic Storage Ring CSR – Mechanical concept and realization. *Nuclear Instruments and Methods in Physics Research Section B: Beam Interactions with Materials and Atoms*, 269(24):2871–2874, 12 2011.

[48] R S Hemsworth, D Boilson, P Blatchford, M Dalla Palma, G Chitarin, H P L de Esch, F Geli, M Dremel, J Graceffa, D Marcuzzi, G Serianni, D Shah, M Singh, M Urbani, and P Zaccaria. Overview of the design of the ITER heating neutral beam injectors. *New Journal of Physics*, 19(2):025005, 2 2017.

[49] O. Shimomura, F. H. Johnson, and Y. Saiga. Extraction, purification and properties of aequorin, a bioluminescent protein from the luminous hydromedusan, Aequorea. *Journal of cellular and comparative physiology*, 59:223–239, 1962.

[50] Lars H. Andersen, Anne P. Rasmussen, Henrik B. Pedersen, Oleg B. Beletsan, and Anastasia V. Bochenkova. High-Resolution Spectroscopy and Selective Photoresponse of Cryogenically Cooled Green Fluorescent Protein Chromophore Anions. *Journal of Physical Chemistry Letters*, 14(28):6395–6401, 7 2023.

[51] L. Vejby-Christensen, D. Kella, D. Mathur, H. B. Pedersen, H. T. Schmidt, and L. H. Andersen. Electron-impact detachment from negative ions. *Physical Review A*, 53(4):2371–2378, 4 1996.

[52] K. Fritioff, J. Sandström, P. Andersson, D. Hanstorp, F. Hellberg, R. Thomas, W. Geppert, M. Larsson, F. Österdahl, G. F. Collins, D. J. Pegg, H. Danared, A. Källberg, and N. D. Gibson. Single and double detachment from H^-. *Physical Review A*, 69(4):042707, 4 2004.

[53] M Allan, O Zatsarinny, and K Bartschat. Electron impact excitation of the ($4p^5 5s$) states in krypton: high-resolution electron scattering experiments and B-spline R-matrix calculations. *Journal of Physics B: Atomic, Molecular and Optical Physics*, 44:65201–65208, 2011.

[54] Moa K. Kristiansson, Kiattichart Chartkunchand, Gustav Eklund, Odd M. Hole, Emma K. Anderson, Nathalie de Ruette, Magdalena Kamińska, Najeeb Punnakayathil, José E. Navarro-Navarrete, Stefan Sigurdsson, Jon Grumer, Ansgar Simonsson, Mikael Björkhage, Stefan Rosén, Peter Reinhed, Mikael Blom, Anders Källberg, John D. Alexander, Henrik Cederquist, Henning Zettergren, Henning T. Schmidt, and Dag Hanstorp. High-precision electron affinity of oxygen. *Nature Communications*, 13(1), 12 2022.

[55] D. Müll, F. Grussie, K. Blaum, S. George, J. Göck, M. Grieser, R. Von Hahn, Z. Harman, Kálosi, C. H. Keitel, C. Krantz, C. Lyu, O. Novotný, F. Nuesslein, D. Paul, V. C. Schmidt, S. Singh, S. Sunil Kumar, X. Urbain, A. Wolf, and H. Kreckel. Metastable states of Si^- observed in a cryogenic storage ring. *Physical Review A*, 104(3), 9 2021.

[56] T. Andersen, H. K. Haugen, and H. Hotop. Binding Energies in Atomic Negative Ions: III. *Journal of Physical and Chemical Reference Data*, 28(6):1511–1533, 1999.

[57] Eugene P. Wigner. On the behavior of cross sections near thresholds. *Physical Review*, 73(9):1002–1009, 1948.

[58] O. Windelius, A. Aguilar, R. C. Bilodeau, A. M. Juarez, I. Rebolledo-Salgado, D. J. Pegg, J. Rohlén, T. Castel, J. Welander, and D. Hanstorp. A collinear angle-resolved photoelectron spectrometer. *Nuclear Instruments and Methods in Physics Research, Section B: Beam Interactions with Materials and Atoms*, 410:144–152, 11 2017.

[59] René C. Bilodeau and Harold K. Haugen. Experimental studies of Os^-: Observation of a bound-bound electric dipole transition in an atomic negative ion. *Physical Review Letters*, 85(3):534–537, 7 2000.

[60] U. Warring, M. Amoretti, C. Canali, A. Fischer, R. Heyne, J. O. Meier, Ch Morhard, and A. Kellerbauer. High-resolution laser spectroscopy on the negative osmium ion. *Physical Review Letters*, 102(4):043001, 1 2009.

[61] A. Fischer, C. Canali, U. Warring, A. Kellerbauer, and S. Fritzsche. First optical hyperfine structure measurement in an atomic anion. *Physical Review Letters*, 104(7):073004, 2 2010.

[62] Lin Pan and Donald R. Beck. Candidates for laser cooling of atomic anions: La^- versus Os^-. *Physical Review A - Atomic, Molecular, and Optical Physics*, 82(1):014501, 7 2010.

[63] C. W. Walter, N. D. Gibson, C. M. Janczak, K. A. Starr, A. P. Snedden, R. L. Field, and P. Andersson. Infrared photodetachment of Ce^-: Threshold spectroscopy and resonance structure. *Physical Review A - Atomic, Molecular, and Optical Physics*, 76(5):052702, 11 2007.

[64] C. W. Walter, N. D. Gibson, Y. G. Li, D. J. Matyas, R. M. Alton, S. E. Lou, R. L. Field, D. Hanstorp, Lin Pan, and Donald R. Beck. Experimental and theoretical study of bound and quasibound states of Ce^-. *Physical Review A - Atomic, Molecular, and Optical Physics*, 84(3):032514, 9 2011.

[65] C. W. Walter, N. D. Gibson, D. J. Matyas, C. Crocker, K. A. Dungan, B. R. Matola, and J. Rohlén. Candidate for laser cooling of a negative ion: Observations of bound-bound transitions in La^-. *Physical Review Letters*, 113(6):063001, 8 2014.

[66] E. Jordan, G. Cerchiari, S. Fritzsche, and A. Kellerbauer. High-Resolution Spectroscopy on the Laser-Cooling Candidate La^-. *Physical Review Letters*, 115(11):113001, 9 2015.

[67] G. Cerchiari, A. Kellerbauer, M. S. Safronova, U. I. Safronova, and P. Yzombard. Ultracold Anions for High-Precision Antihydrogen Experiments. *Physical Review Letters*, 120(13):133205, 3 2018.

[68] Rulin Tang, Ran Si, Zejie Fei, Xiaoxi Fu, Yuzhu Lu, Tomas Brage, Hongtao Liu, Chongyang Chen, and Chuangang Ning. Candidate

for Laser Cooling of a Negative Ion: High-Resolution Photoelectron Imaging of Th^-. *Physical Review Letters*, 123(20):203002, 11 2019.

[69] Michael Scheer, Cicely A. Brodie, René C. Bilodeau, and Harold K. Haugen. Laser spectroscopic measurements of binding energies and fine-structure splittings of Co^-, Ni^-, Rh^-, and Pd^-. *Physical Review A*, 58(3):2051–2062, 9 1998.

[70] K. R. Lykke, K. K. Murray, and W. C. Lineberger. Threshold photodetachment of H^-. *Physical Review A*, 43(11):6104–6107, 6 1991.

[71] W H King. *ISOTOPE SHIFTS IN ATOMIC SPECTRA*. Springer Science+Business Media New York, New York, 1984.

[72] U Berzinsh, M Gustafsson, D Hanstorp, A Klinkmüller, U Ljungblad, and A.-M Martensson-Pendrill. Isotope shift in the electron affinity of chlorine. Technical Report 1, 1994.

[73] David Bresteau, Cyril Drag, and Christophe Blondel. Isotope shift of the electron affinity of carbon measured by photodetachment microscopy. *Physical Review A*, 93(1):013414, 1 2016.

[74] C. Blondel, C. Delsart, C. Valli, S. Yiou, M. R. Godefroid, and S. Van Eck. Electron affinities of ^{16}O, ^{17}O, ^{18}O, the fine structure of $^{16}O^-$, and the hyperfine structure of $^{17}O^-$. *Physical Review A*, 64(5):052504, 10 2001.

[75] Moa Kristiansson. *Precision measurements on negative ions*. PhD thesis, Stockholm, 2022.

[76] Thomas Carette, Cyril Drag, Oliver Scharf, Christophe Blondel, Christian Delsart, Charlotte Froese Fischer, and Michel Godefroid. Isotope shift in the sulfur electron affinity: Observation and theory. *Physical Review A*, 81(4):042522, 4 2010.

[77] S. Rothe, J. Sundberg, J. Welander, K. Chrysalidis, T.D. Goodacre, V. Fedosseev, S. Fiotakis, O. Forstner, R. Heinke, K. Johnston, T. Kron, U. Köster, Y. Liu, B. Marsh, A. Ringvall-Moberg, R.E. Rossel, C. Seiffert, D. Studer, K. Wendt, and D. Hanstorp. Laser photodetachment of radioactive $^{128}I^-$. *Journal of Physics G: Nuclear and Particle Physics*, 44(10), 2017.

[78] C Froese Fischer, G Gaigalas, and P Jönsson. GRASP2018-A Fortran 95 version of the General Relativistic Atomic Structure Package. *Z. Rudzikas, Atomic Data and Nuclear Data Tables*, 237:235, 2019.

[79] Michael Scheer, René C. Bilodeau, Cicely A. Brodie, and Harold K. Haugen. Systematic study of the stable states of C^-, Si^-, Ge^-, and Sn^- via infrared laser spectroscopy. *Physical Review A*, 58(4):2844–2856, 10 1998.

[80] A Kasdan, E Herbst, and W C Lineberger. Laser photoelectron spectrometry of the negative ions of silicon and its hydrides. *J. Chem. Phys*, 62:541, 1975.

[81] W Chaibi, R J Peláez, C Blondel, C Drag, and C Delsart. Effect of a magnetic field in photodetachment microscopy. *Eur. Phys. J. D*, 58:29–37, 2010.

[82] J. Warbinek, D. Leimbach, D. Lu, K. Wendt, D. J. Pegg, A. Yurgens, D. Hanstorp, and J. Welander. A graphene-based neutral particle detector. *Applied Physics Letters*, 114(6), 2 2019.

[83] R. Catherall, W. Andreazza, M. Breitenfeldt, A. Dorsival, G. J. Focker, T. P. Gharsa, T. J. Giles, J. L. Grenard, F. Locci, P. Martins, S. Marzari, J. Schipper, A. Shornikov, and T. Stora. The ISOLDE facility. *Journal of Physics G: Nuclear and Particle Physics*, 44(9), 8 2017.

[84] Y. Liu, D. W. Stracener, and T. Stora. Production of negatively charged radioactive ion beams. *New Journal of Physics*, 19(8), 8 2017.

[85] David Leimbach, Julia Karls, Yangyang Guo, Rizwan Ahmed, Jochen Ballof, Lars Bengtsson, Ferran Boix Pamies, Anastasia Borschevsky, Katerina Chrysalidis, Ephraim Eliav, Dmitry Fedorov, Valentin Fedosseev, Oliver Forstner, Nicolas Galland, Ronald Fernando Garcia Ruiz, Camilo Granados, Reinhard Heinke, Karl Johnston, Agota Koszorus, Ulli Köster, Moa K. Kristiansson, Yuan Liu, Bruce Marsh, Pavel Molkanov, Lukáš F. Pašteka, João Pedro Ramos, Eric Renault, Mikael Reponen, Annie Ringvall-Moberg,

Ralf Erik Rossel, Dominik Studer, Adam Vernon, Jessica Warbinek, Jakob Welander, Klaus Wendt, Shane Wilkins, Dag Hanstorp, and Sebastian Rothe. The electron affinity of astatine. *Nature Communications*, 11(1), 12 2020.

[86] D. Leimbach, S. Rothe, L. Bengtsson, A. Ringvall-Moberg, J. Sundberg, K. Wendt, and D. Hanstorp. Upgrades of the GANDALPH photodetachment detector towards the determination of the electron affinity of astatine. *Nuclear Instruments and Methods in Physics Research, Section B: Beam Interactions with Materials and Atoms*, 463, 2020.

[87] P. F. Moulton. Spectroscopic and laser characteristics of Ti:Al_2O_3. *Journal of the Optical Society of America B*, 3(1):125, 1 1986.

[88] J. A. Giordmaine and Robert C. Miller. Tunable Coherent Parametric Oscillation in $LiNbO_3$ at Optical Frequencies. *Physical Review Letters*, 14(24):973–976, 6 1965.

[89] B H Soffer and B B Mcfarland. Continuously tunable, narrow-band organic dye lasers. *Appl. Phys. Lett*, 10:266, 1967.

[90] S. Rothe, B. A. Marsh, C. Mattolat, V. N. Fedosseev, and K. Wendt. A complementary laser system for ISOLDE RILIS. In *Journal of Physics: Conference Series*, volume 312. Institute of Physics Publishing, 2011.

[91] R. D. Thomas, H. T. Schmidt, G. Andler, M. Björkhage, M. Blom, L. Brännholm, E. Bäckström, H. Danared, S. Das, N. Haag, P. Halldén, F. Hellberg, A. I.S. Holm, H. A.B. Johansson, A. Källberg, G. Källersjö, M. Larsson, S. Leontein, L. Liljeby, P. Löfgren, B. Malm, S. Mannervik, M. Masuda, D. Misra, A. Orbán, A. Pal, P. Reinhed, K. G. Rensfelt, S. Rosén, K. Schmidt, F. Seitz, A. Simonsson, J. Weimer, H. Zettergren, and H. Cederquist. The double electrostatic ion ring experiment: A unique cryogenic electrostatic storage ring for merged ion-beams studies. *Review of Scientific Instruments*, 82(6), 6 2011.

[92] R. Middleton. A versatile high intensity negative ion source. *Nuclear Instruments and Methods in Physics Research*, 214(2-3):139–150, 9 1983.

[93] National Electrostatics Corporation. Source of Negative Ions by Cesium Sputtering-SNICS II. Technical report, National Electrostatic Corporation, USA.

[94] M. L. Yu. Work-Function Dependence of Negative-Ion Production during Sputtering. *Phys. Rev. Lett.*, 40:574–577, 2 1978.

[95] R. Honig and H. Hook. Vapor pressure data for some common gases. *RCA Review*, 21(3):360–368, 1960.

[96] M Squared. `www.m2lasers.com`. Accessed: 2023-12-29.

[97] A. Ringvall-Moberg et al. The electron affinity of rubidium: A state selective measurement. *In manuscript*, 2024.

[98] J. Welander, J. E. Navarro Navarrete, J. Rohlén, T. Leopold, R. D. Thomas, D. J. Pegg, and D. Hanstorp. A field ionizer for photodetachment studies of negative ions. *Review of Scientific Instruments*, 93(6), 6 2022.

[99] Christophe Blondel, Christian Delsart, and Fabienne Goldfarb. Electron spectrometry at the µeV level and the electron affinities of Si and F. *Journal of Physics B: Atomic, Molecular and Optical Physics*, 34(9):L281–L288, 5 2001.

[100] C. Blondel, W. Chaibi, C. Delsart, C. Drag, F. Goldfarb, and S. Kröger. The electron affinities of O, Si, and S revisited with the photodetachment microscope. *European Physical Journal D*, 33(3):335–342, 2005.

[101] L.A. Schaller, T. Dubler, K. Kaeser, G.A. Rinker, B. Robert-Tissot, L. Schellenberg, and H. Schneuwly. Nuclear charge radii from muonic X-ray transitions in F, Na, Al, Si, P, S and K. *Nuclear Physics A*, 300(2):225–234, 5 1978.

[102] R. J. Pelez, C. Blondel, C. Delsart, and C. Drag. Pulsed photodetachment microscopy and the electron affinity of iodine. *Journal of Physics B: Atomic, Molecular and Optical Physics*, 42(12), 2009.

[103] R. Engleman, R. A. Keller, and B. A. Palmer. Hyperfine structure and isotope shift of the 13-μm transition of ^{129}I. *Applied Optics*, 19(16):2767, 8 1980.

[104] P Juncar, C R Bingham, J A Bounds, D J Pegg, H K Carter, R L Mlekodaj, and J D Cole. New Method to Measure the Relativistic Doppler Shift: First Results and a Proposal. Technical report, 1985.

[105] S. Rothe, A. N. Andreyev, S. Antalic, A. Borschevsky, L. Capponi, T. E. Cocolios, H. De Witte, E. Eliav, D. V. Fedorov, V. N. Fedosseev, D. A. Fink, S. Fritzsche, L. Ghys, M. Huyse, N. Imai, U. Kaldor, Yuri Kudryavtsev, U. Köster, J. F.W. Lane, J. Lassen, V. Liberati, K. M. Lynch, B. A. Marsh, K. Nishio, D. Pauwels, V. Pershina, L. Popescu, T. J. Procter, D. Radulov, S. Raeder, M. M. Rajabali, E. Rapisarda, R. E. Rossel, K. Sandhu, M. D. Seliverstov, A. M. Sjödin, P. Van Den Bergh, P. Van Duppen, M. Venhart, Y. Wakabayashi, and K. D.A. Wendt. Measurement of the first ionization potential of astatine by laser ionization spectroscopy. *Nature Communications*, 4, 2013.

[106] Robert S. Mulliken. A new electroaffinity scale; Together with data on valence states and on valence ionization potentials and electron affinities. *The Journal of Chemical Physics*, 2(11):782–793, 1934.

[107] Brian A Finney and Kirk A Peterson. Beyond chemical accuracy in the heavy p-block: The first ionization potentials and electron affinities of Ga–Kr, In–Xe, and Tl–Rn. *The Journal of Chemical Physics*, 151(2):024303, 7 2019.

[108] R. Si and C. Froese Fischer. Electron affinities of At and its homologous elements Cl, Br, and I. *Physical Review A*, 98(5):052504, 11 2018.

[109] Dumitru Claudiu Sergentu, Grégoire David, Gilles Montavon, Rémi Maurice, and Nicolas Galland. Scrutinizing "invisible" astatine: A challenge for modern density functionals. *Journal of Computational Chemistry*, 37(15):1345–1354, 2016.

[110] A. Borschevsky, L. F. Pašteka, V. Pershina, E. Eliav, and U. Kaldor. Ionization potentials and electron affinities of the superheavy elements 115-117 and their sixth-row homologues Bi, Po, and at. *Physical Review A - Atomic, Molecular, and Optical Physics*, 91(2):1–5, 2015.

[111] Junqin Li, Zilong Zhao, Martin Andersson, Xuemei Zhang, and Chongyang Chen. Theoretical study for the electron affinities of negative ions with the MCDHF method. *Journal of Physics B: Atomic, Molecular and Optical Physics*, 45(16), 8 2012.

[112] Marie L. Laury and Angela K. Wilson. Examining the heavy p-block with a pseudopotential-based composite method: Atomic and molecular applications of rp-ccCA. *Journal of Chemical Physics*, 137(21), 2012.

[113] Zhiwei Chang, Jiguang Li, and Chenzhong Dong. Ionization Potentials, Electron Affinities, Resonance Excitation Energies, Oscillator Strengths, And Ionic Radii of Element Uus (Z = 117) and Astatine. *The Journal of Physical Chemistry A*, 114(51):13388–13394, 12 2010.

[114] Tao Zeng, Dmitri G. Fedorov, and Mariusz Klobukowski. Multireference study of spin-orbit coupling in the hydrides of the 6p-block elements using the model core potential method. *Journal of Chemical Physics*, 132(7), 2010.

[115] Alexander V. Mitin and Christoph Van Wüllen. Two-component relativistic density-functional calculations of the dimers of the halogens from bromine through element 117 using effective core potential and all-electron methods. *Journal of Chemical Physics*, 124(6), 2006.

[116] Björn O. Roos, Roland Lindh, Per Åke Malmqvist, Valera Veryazov, and Per Olof Widmark. Main Group Atoms and Dimers Studied with a New Relativistic ANO Basis Set. *Journal of Physical Chemistry A*, 108(15):2851–2858, 2004.

[117] Kirk A. Peterson. Systematically convergent basis sets with relativistic pseudopotentials. I. Correlation consistent basis sets for the post- ¡i¿d¡/i¿ group 13–15 elements. *The Journal of Chemical Physics*, 119(21):11099–11112, 12 2003.

[118] R. J. Zollweg. Electron affinities of the heavy elements. *The Journal of Chemical Physics*, 50(10):4251–4261, 1969.

[119] P Frey, F Breyer, and H Holop. High resolution photodetachment from the rubidium negative ion around the Rb($5p_{1/2}$) threshold. *Journal of Physics B: Atomic and Molecular Physics*, 11(19):L589–L594, 10 1978.

[120] J. E. Sansonetti. Wavelengths, transition probabilities, and energy levels for the spectra of rubidium (Rb i through Rb XXXVII). *Journal of Physical and Chemical Reference Data*, 35(1):301–421, 2006.

[121] Constantine E. Theodosiou. Lifetimes of alkali-metal—atom Rydberg states. *Physical Review A*, 30(6):2881–2909, 12 1984.

[122] René C. Bilodeau, Michael Scheer, Harold K. Haugen, and Robert L. Brooks. Near-threshold laser spectroscopy of iridium and platinum negative ions: Electron affinities and the threshold law. *Physical Review A*, 61(1):012505, 12 1999.

[123] Yuzhu Lu, Jing Zhao, Rulin Tang, Xiaoxi Fu, and Chuangang Ning. Measurement of electron affinity of iridium atom and photoelectron angular distributions of iridium anion. *Journal of Chemical Physics*, 152(3), 1 2020.

[124] M. K. Kristiansson, S. Schiffmann, J. Grumer, J. Karls, N. de Ruette, G. Eklund, V. Ideböhn, N. D. Gibson, T. Brage, H. Zettergren, D. Hanstorp, and H. T. Schmidt. Experimental and theoretical studies of excited states in Ir^-. *Physical Review A*, 103(6):062806, 6 2021.

[125] J. Thøgersen, M. Scheer, L. D. Steele, H. K. Haugen, and W. P. Wijesundera. Two-Photon Detachment of Negative Ions via Magnetic Dipole Transitions. *Physical Review Letters*, 76(16):2870–2873, 4 1996.

[126] C. S. Feigerle, R. R. Corderman, S. V. Bobashev, and W. C. Lineberger. Binding energies and structure of transition metal negative ions. *The Journal of Chemical Physics*, 74(3):1580–1598, 1980.

[127] Yangluojia Su, Ran Si, Ke Yao, and Tomas Brage. The structure and radiative lifetimes of negative ions homologous to N^-. *Journal of Physics B: Atomic, Molecular and Optical Physics*, 52(12), 2019.

[128] M. K. Kristiansson, J. Karls, N. D. Gibson, D. Hanstorp, H. T. Schmidt, and C. W. Walter. Measurement of the lifetime of a metastable excited state in Bi^-. *Physical Review A*, 105(1):L010801, 1 2022.

[129] Steven M. O'Malley and Donald R. Beck. Lifetimes and branching ratios of excited states in La^-, Os^-, Lu^-, Lr^-, and Pr^-. *Physical Review A*, 81(3):032503, 3 2010.

[130] Christophe Blondel. Comment on "Measurement of the electron affinity of the lanthanum atom". *Physical Review A*, 101(1):016501, 1 2020.

[131] Yuzhu Lu, Rulin Tang, Xiaoxi Fu, and Chuangang Ning. Measurement of the electron affinity of the lanthanum atom. *Physical Review A*, 99(6):062507, 6 2019.

[132] N. D. Gibson et al. Lifetimes of excited states of the lanthanum negative ion. *In manuscript*, 2024.

[133] Martin Martschini, Johannes Lachner, Silke Merchel, Alfred Priller, Peter Steier, Anton Wallner, Alexander Wieser, and Robin Golser. The quest for AMS of ^{182}Hf - why poor gas gives pure beams. *EPJ Web of Conferences*, 232:02003, 4 2020.

[134] Hubert Gnaser, Martin Martschini, David Leimbach, Julia Karls, Dag Hanstorp, Suvasthika Indrajith, Mingchao Ji, Paul Martini, Ansgar Simonsson, Henning Zettergren, Henning T. Schmidt, and Robin Golser. Spontaneous and photo-induced decay processes of WF_5^- And HfF_5^- Molecular anions in a cryogenic storage ring. *Journal of Chemical Physics*, 157(4), 7 2022.

[135] Hongshan Chen, Pontus Andersson, Anton O. Lindahl, and Dag Hanstorp. The electronic structure of $HfF5^-$ and $WF5^-$. *Chemical Physics Letters*, 511(4-6):196–200, 8 2011.

[136] Junqin Li, Zilong Zhao, Martin Andersson, Xuemei Zhang, and Chongyang Chen. Theoretical study for the electron affinities of negative ions with the MCDHF method. *Journal of Physics B: Atomic, Molecular and Optical Physics*, 45(16), 2012.

[137] C. W. Walter, N. D. Gibson, D. J. Matyas, C. Crocker, K. A. Dungan, B. R. Matola, and J. Rohlén. Candidate for laser cooling of a negative ion: Observations of bound-bound transitions in la. *Physical Review Letters*, 113(6), 8 2014.